An Airborne Radar Model For
Non-Uniformly Spaced Antenna Arrays

THESIS

Matthew V. Young, Second Lieutenant, USAF

AFIT-GE-ENG-06-58

DEPARTMENT OF THE AIR FORCE
AIR UNIVERSITY

AIR FORCE INSTITUTE OF TECHNOLOGY

Wright-Patterson Air Force Base, Ohio

AFIT-GE-ENG-06-58

An Airborne Radar Model For Non-Uniformly Spaced Antenna Arrays

THESIS

Presented to the Faculty

Department of Electrical and Computer Engineering

Graduate School of Engineering and Management

Air Force Institute of Technology

Air University

Air Education and Training Command

In Partial Fulfillment of the Requirements for the

Degree of Master of Science in Electrical Engineering

Matthew V. Young, BS

Second Lieutenant, USAF

March 2006

AFIT-GE-ENG-06-58

An Airborne Radar Model For Non-Uniformly Spaced Antenna Arrays

Matthew V. Young, BS

Second Lieutenant, USAF

Approved:

/signed/	6 Mar 2006
Maj. Todd B. Hale (Chairman)	Date
/signed/	6 Mar 2006
Dr. Michael A. Temple (Member)	Date
/signed/	6 Mar 2006
Dr. Richard K. Martin (Member)	Date

AFIT-GE-ENG-06-58

Abstract

     This thesis presents an airborne radar model for non-uniformly spaced antenna arrays. An airborne radar model for non-uniformly spaced arrays is important because the performance of arbitrary array configurations can be analyzed. Non-uniformly spaced arrays could potentially possess advantages which are unobtainable with uniformly spaced arrays. First, an element position matrix is defined to accommodate arbitrary element locations. The new element position matrix produces changes to the time/phase delay to each element, the spatial frequencies, the steering vectors, the space-time snapshots, and the covariance matrices. The joint domain localized (JDL) and factored time-space (FTS) STAP algorithms are also updated so they are compatible with the model for non-uniformly spaced arrays. The non-uniformly spaced array radar model presented is verified with previous models presented by Jaffer [6], Ward [13], and Hale [5]. Past research involving non-uniform arrays mostly addressed circular arrays, particularly the ultra high frequency (UHF) Electronically Scanned Array developed by the Office of Naval Research. Therefore, the model for non-uniform arrays is used to evaluate performance of two different circular arrays, one containing 24 elements and one containing 15 elements. The circular array performance is compared to that of a 6×6 uniformly spaced planar array having the same dimensions. Signal-to-interference plus noise ratio (SINR) loss and detection probability metrics are used to evaluate array performance. Array failure is also examined using output SINR plots for each array. Simulation results indicate that non-uniformly spaced arrays such as the circular array can potentially be used in airborne radar systems in place of uniformly spaced arrays. As a result, array costs may be reduced by using fewer elements without sacrificing detection capabilities.

Acknowledgements

I would like to thank my thesis advisor, Major Hale, for all of his guidance. I have learned a lot as a result of his high standards. Next, I would like to thank the other faculty members on my thesis committee, Dr. Michael Temple and Dr. Richard Martin, for taking the time to be on my thesis committee. They have also aided in my learning experience at AFIT as teachers. Lastly, I would like to thank all the students that have helped me make it through my classes. Their help on homework assignments and projects has greatly aided in learning subject material more quickly. The knowledge acquired from this experience at AFIT has left me feeling greatly rewarded.

Matthew V. Young

Table of Contents

List of Figures

x

List of Tables

List of Symbols

List of Abbreviations

An Airborne Radar Model For
Non-Uniformly Spaced Antenna Arrays

I. Introduction

Non-uniformly spaced antenna arrays are studied because they may be used with space-time adaptive processing (STAP) techniques in airborne radar systems in the near future. Non-uniformly spaced arrays are a topic of interest since they may have certain advantageous characteristics not possessed by uniform arrays. For example, circular arrays can be electronically scanned 360° in azimuth, whereas uniform arrays must be mechanically steered. Circular arrays are becoming more popular since they can be easily implemented in the nose of an aircraft [7]. Some non-uniform array configurations may also provide lower sidelobes than uniformly spaced arrays. Another possible advantage of non-uniformly spaced arrays is the use of fewer elements. Array costs can be reduced if fewer elements are arranged non-uniformly while maintaining the same detection performance as uniformly spaced arrays. In some cases, uniform spacing of elements may not be feasible. There might be limited space on a platform, so an antenna array may have to conform around certain components or other obstacles on the platform. Non-uniformly spaced arrays are also investigated to see if they are more or less susceptible to element failure than the uniformly spaced array.

1.1 Objectives

The primary objective of this thesis is to develop a radar model for arrays with any element spacing, uniform or non-uniform. The radar data model for linear arrays developed by Ward [13] and Jaffer [6] and extended to planar arrays by Hale [5] is modified to include non-uniform element spacing for linear, planar, and three-dimensional arrays. However, the model derived in this thesis does not account for shadowing effects that may occur in the three-dimensional array. Shadowing occurs when some elements in the array do not receive the incoming radar wave due to their location.

1

The modifications to the radar model begin by redefining the element position vector as an element position matrix. The new element position matrix trickles through the radar model, bringing about many changes. The new element position matrix affects the time/phase delay to each element, the spatial frequencies, the steering vectors, the space-time snapshots, the array pattern, and the covariance matrices. The joint domain localized (JDL) and factored time-space (FTS) STAP algorithms are also modified to reflect the changes due to non-uniform element spacing. These changes affect output signal-to-interference plus noise ratio (SINR), SINR loss, and detection probability. Grating lobes may also result from non-uniform element spacing, depending on the array configuration.

Once a model for non-uniform element spacing is developed, the next objective is to ensure it is correct. To verify it is correct, uniform element spacing is inserted into the model and compared to the radar model of [5, 6, 13]. The two models are mathematically equivalent when the uniformly spaced array is linear. The two models are structured differently for the uniformly spaced planar array case. Therefore, simulations are performed to verify the same results are produced from each model.

1.2   Performance Evaluation

This thesis also intends to determine the impact of non-uniform element spacing on adaptive interference suppression techniques. The performance of non-uniformly spaced arrays and uniformly spaced arrays is compared to determine if certain non-uniform array configurations can be used in place of uniform arrays. Two different non-uniform arrays are used for experimentation to characterize their performance. The non-uniform arrays used include a 15 element circular array and a 24 element circular array. The STAP techniques used in the simulations are the JDL and FTS methods. JDL and FTS are used because they are practical STAP methods that can be implemented in real-world radar systems due to their reduced sample support. The matched filter is also used in simulations as the ideal performance bound for each

STAP method. The performance of each array is compared to evaluate the impact of different element configurations.

Array performance is evaluated based on a variety of simulations. The antenna pattern is plotted first to examine the energy radiated from the array. The antenna pattern shows features such as sidelobes, backlobes, and nulls. Next, the clutter covariance matrix eigenvalues are plotted to examine the element configuration impact on clutter rank. Covariance matrices describe the expected signal power returns from sources such as clutter, noise, jammers, or targets. A matrix with high rank means there is weak correlation between samples. For example, the white noise covariance matrix is full rank because white noise is completely uncorrelated from sample to sample. The jammer and clutter matrices have low ranks due to correlation between samples. The physical meaning of low clutter matrix rank is new incoming data samples do not offer much more information about the clutter environment than previous samples. The power spectra of each array is plotted using the signal match and minimum variance estimator (MVE) algorithms to examine the interference environment. The signal match method shows the interference as illuminated by the array. Therefore, interference due to sidelobes and grating lobes is contained in the signal match power spectra. The MVE power spectra simply shows where the interference is physically located relative to the radar. The performance of each array using STAP techniques is finally evaluated with SINR loss and detection probability plots. SINR loss is the actual output SINR referenced to the maximum output signal-to-noise ratio (SNR). SINR loss is plotted to compare array performance since each array has a different number of elements, resulting in a different output SINR. SINR loss is plotted versus normalized Doppler frequency for the matched filter, FTS, and JDL methods. Detection probability is plotted versus input SINR per element per pulse for the adaptive matched filter (AMF), JDL, and FTS methods. The SINR loss and detection probability plots characterize the performance of each array for each STAP method. Finally, array failure is briefly examined using output SINR plots for each array with 0%, 10%, and 20% element failure rates.

1.3 Organization

This thesis is broken down into six chapters. Chapter I introduces the problem and research goals. A brief overview of how the problem is to be solved is also discussed. Chapter II discusses the radar data models presented in [5, 6, 13]. These models are for uniformly spaced arrays. A few different STAP algorithms discussed in [5, 12, 13] are also mentioned in Chapter II since they are used in simulations in the following chapters. Chapter III shows the development incorporating non-uniform element spacing into the radar model of [5]. Spatial frequencies, steering vectors, space-time snapshots, covariance matrices, and two STAP algorithms are updated to reflect the necessary changes. The model presented in Chapter III is verified in Chapter IV to ensure it is correct. Verification is done by inserting uniform element spacing into the model presented in Chapter III and comparing it to the model in [5,6,13]. First, the uniform linear array is verified mathematically. Then, the planar array is verified via simulation since the variables are structured differently between each model. Simulation plots and results are presented in Chapter V to evaluate the performance of each array. SINR loss, output SINR, detection probability, clutter rank, and power spectra plots are the simulations used for evaluation. Chapter VI draws conclusions based on the simulation results. Future research is also discussed in this chapter.

1.4 Notation

All notation in this thesis follows the standard technical writing convention. Scalar values are symbols in regular font. For example, θ is the elevation angle and ϕ is the azimuth angle. Column vectors are represented by lower case bold symbols. The temporal steering vector $\mathbf{b}$ and the space-time steering vector $\mathbf{v}$ are examples of column vectors. Matrices are represented by upper case bold symbols. For example, $\mathbf{R}$ is the covariance matrix. Identity matrices always have subscripts denoting their dimensions. An identity matrix of size $NM \times NM$ is written $\mathbf{I}_{NM}$. The Hermitian is the complex conjugate transpose and is denoted by a superscript H as in $\mathbf{R}^H$. A

transformed vector or matrix has a tilde over it. The vector $\tilde{\boldsymbol{\chi}}$ is $\boldsymbol{\chi}$ projected into a different space. Estimated quantities and unit vectors have hats over them. For example, $\hat{\mathbf{R}}$ is an estimate of the covariance matrix $\mathbf{R}$ while $\hat{x}$ is a unit vector in the x direction. Careful attention must be paid to the context to distinguish which operation the hat is being used for. The expected value operator is written as $\varepsilon\{\cdot\}$.

II.   Past Research In STAP For Airborne Radar

T his chapter examines past research efforts involving the model for an airborne radar and STAP algorithms for that model. A model for radar system analysis is presented in [6, 13] for a sidelooking uniform linear array. That model was later extended in [5] for a uniform planar array containing P rows of uniformly spaced N element linear arrays. That radar model is discussed here because it is modified in the following chapter to allow non-uniform element spacing.

2.1   Airborne Radar Model

2.1.1   Array Geometry.   The radar model in [5] begins with the physical geometry of the antenna shown in Fig. 2.1. The elements are divided into P rows along the z-axis and N columns along the x-axis. The space between each element is denoted as d_x along the x-axis and d_z along the z-axis. The location of element np is defined as

$$\mathbf{d}_{np} = -nd_x\hat{\mathbf{x}} - pd_z\hat{\mathbf{z}}, \tag{2.1}$$

where $\hat{\mathbf{x}}$ and $\hat{\mathbf{z}}$ are unit vectors in the x and z directions, respectively. The array geometry affects every aspect of the radar model.
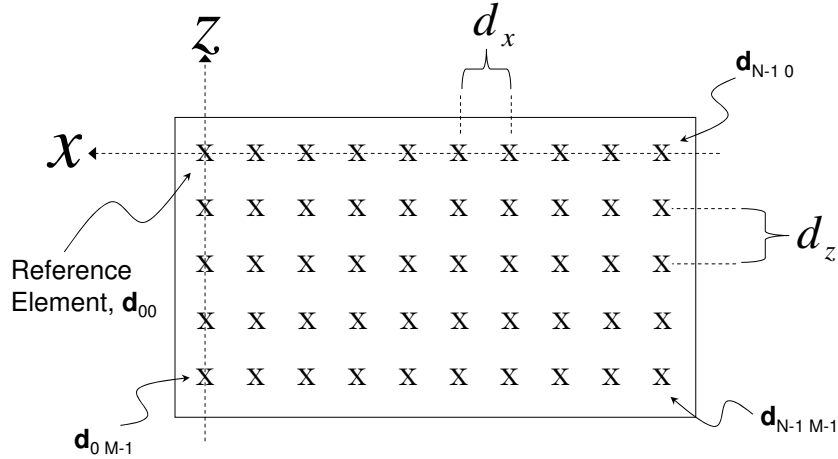
Figure 2.1:   Sidelooking uniformly spaced planar array lying in the xz-plane. The reference element is located at the origin. The aircraft velocity vector is along the positive x-axis.

2.1.2 Received Signal. The received signal time/phase delay to each array element changes based on the array geometry. The time delay to the np^{th} element is

$$
\begin{aligned}
\tau'_{np} &= \frac{\hat{\mathbf{k}}(\theta, \phi) \cdot \mathbf{d}_{np}}{c} \\
&= \frac{-nd_x \cos\theta \sin\phi - pd_z \sin\theta}{c}.
\end{aligned}
\tag{2.2}
$$

The resulting spatial frequency ϑ for a target located at azimuth angle ϕ and elevation angle θ also changes based on the array geometry. The spatial frequency is divided into an x-component

$$
\vartheta_x = \frac{d_x \cos\theta \sin\phi}{\lambda_o}
\tag{2.3}
$$

and z-component

$$
\vartheta_z = \frac{d_z \sin\theta}{\lambda_o}
\tag{2.4}
$$

when the array is uniformly spaced. A uniformly spaced planar array can have two spatial steering vectors, one for azimuth and one for elevation, to locate a target in space. The azimuth steering vector $\mathbf{a}$ and elevation steering vector $\mathbf{e}$ are defined as

$$
\mathbf{a}(\vartheta_x) = [1 \ \ e^{j2\pi\vartheta_x} \ \ \cdots \ \ e^{j2\pi(N-1)\vartheta_x}]^T
\tag{2.5}
$$

and

$$
\mathbf{e}(\vartheta_z) = [1 \ \ e^{j2\pi\vartheta_z} \ \ \cdots \ \ e^{j2\pi(P-1)\vartheta_z}]^T.
\tag{2.6}
$$

The temporal steering vector

$$
\mathbf{b}(\bar{\omega}) = [1 \ \ e^{j2\pi\bar{\omega}} \ \ \cdots \ \ e^{j2\pi(M-1)\bar{\omega}}]^T
\tag{2.7}
$$

is used with the spatial steering vectors to construct the 3D steering vector to a specific azimuth angle, elevation angle, and normalized Doppler frequency $\bar{\omega}$ as

$$
\mathbf{v}(\vartheta_z, \bar{\omega}, \vartheta_x) = \mathbf{e}(\vartheta_z) \otimes \mathbf{b}(\bar{\omega}) \otimes \mathbf{a}(\vartheta_x).
\tag{2.8}
$$

7

The Kronecker Product $\otimes$ is described in Appendix A and M is the number of pulses. The space-time snapshot $\boldsymbol{\chi}_t$ representing the target return is simply the 3D steering vector scaled by a complex value

$$\boldsymbol{\chi}_t = \alpha_t \mathbf{v}(\vartheta_z, \bar{\omega}, \vartheta_x). \tag{2.9}$$

2.1.3 Array Factor.   The array factor is necessary to construct the correct transmit pattern from the array. The array factor is required for clutter and jammer modelling since it dictates the energy amplitude and location in azimuth and elevation. The array factor is the sum of all weights over the array and is defined as

$$W(\theta, \phi) = [\mathbf{e}(\vartheta_z) \otimes \mathbf{a}(\vartheta_x)]^T \mathbf{1} \tag{2.10}$$

in [5] where $\mathbf{1}$ is a vector of ones. Equation (2.10) is the array factor for a mainbeam steered to boresight. The mainbeam can be steered to any azimuth and elevation by

$$W(\theta, \phi) = [\mathbf{e}(\vartheta_z) \otimes \mathbf{a}(\vartheta_x)]^H [\mathbf{e}(\vartheta'_z) \otimes \mathbf{a}(\vartheta'_x)], \tag{2.11}$$

where ϑ'_x and ϑ'_z contain the mainbeam azimuth and elevation location. See [1,11] for more information on array beamforming.

2.1.4 Jammer Model.   The jammer modelled in [5, 6, 13] is a barrage noise jammer. This barrage noise jammer model is briefly mentioned here and is discussed in greater detail in Chapter III. The jammer space-time snapshot is

$$\boldsymbol{\chi}_j = \mathbf{e}(\vartheta_z) \otimes \boldsymbol{\alpha}_j \otimes \mathbf{a}(\vartheta_x) \tag{2.12}$$

where

$$\boldsymbol{\alpha}_j = [\alpha_0 \ \alpha_1 \ \cdots \ \alpha_{M-1}]^T \tag{2.13}$$

8

is a vector representing the complex random jammer amplitudes received from each pulse. A barrage noise jammer has no temporal correlation since its amplitude varies from pulse to pulse. The jammer covariance matrix is constructed from its space-time snapshot as

$$\mathbf{R}_j = \varepsilon\{\boldsymbol{\chi}_j \boldsymbol{\chi}_j^H\}. \tag{2.14}$$

2.1.5 Clutter Model.   The clutter model in [5,6,13] is briefly mentioned here since it is discussed in greater detail in the following chapter. A constant gamma model for ground clutter is the clutter model basis. The clutter space-time snapshot is

$$\boldsymbol{\chi}_c = \sum_{i=0}^{N_r-1} \sum_{k=0}^{N_c-1} \alpha_{ik} \mathbf{e}(\vartheta_z) \otimes \mathbf{b}(\bar{\omega}_{ik}) \otimes \mathbf{a}(\vartheta_x), \tag{2.15}$$

where α_{ik} is the clutter patch amplitude and ϑ_z and ϑ_x contain the elevation angle θ_i and azimuth angle ϕ_k to the clutter patch. The clutter patch normalized Doppler frequency $\bar{\omega}$ is

$$
\begin{aligned}
\bar{\omega}_{ik} &= \frac{f_c(\theta_i, \phi_k)}{f_r} = f_c(\theta_i, \phi_k) T_r \\
&= \beta \vartheta_x = \frac{2 v_a T_r}{d_x} \vartheta_x,
\end{aligned} \tag{2.16}
$$

where f_c is the Doppler frequency, f_r is the pulse repetition frequency (PRF), T_r is the pulse repetition interval (PRI), and v_a is the aircraft speed. Equation (2.16) shows the normalized Doppler frequency dependence on azimuth angle with a slope β describing the number of half-interelement spacings d_x crossed during one PRI. The value of β determines how difficult it is to suppress clutter. If β is greater than one, clutter spatial frequencies are spread over a frequency band greater than the PRF, resulting in Doppler ambiguous clutter returns. In other words, different clutter patches can have the same Doppler frequency as each other. The final portion of the clutter model is the covariance matrix

$$\mathbf{R}_c = \varepsilon\{\boldsymbol{\chi}_c \boldsymbol{\chi}_c^H\}. \tag{2.17}$$

The clutter model is important because it describes the interference from the environment around the radar platform.

2.2 Performance Metrics

A few different performance metrics are used to characterize the performance of an array. These metrics include output SINR, SINR loss, and detection probability. The signal match and MVE methods are two different spectral estimation techniques used to examine the interference environment.

2.2.1 Output SINR. Output SINR is described in [13] as a common metric used to characterize processor performance. It is a ratio of output target power to interference plus noise power. SINR is given as

$$\text{SINR} = \frac{\sigma^2 \xi_t |\mathbf{w}^H \mathbf{v}|^2}{\mathbf{w}^H \mathbf{R} \mathbf{w}} \tag{2.18}$$

in [5], where ξ_t is the target SNR per element per pulse, σ^2 is the noise power per element per pulse, and $\mathbf{w}$ is the weight vector. SINR is plotted as a function of normalized target Doppler frequency since target velocity is not known. Output SINR changes based on the number of elements in the array. Arrays with more elements have a higher output SINR than arrays with fewer elements.

2.2.2 SINR Loss. SINR loss is another performance metric described in [13]. It is valuable because it shows the losses due to interference suppression, filter straddling losses, and taper losses. Therefore, interference suppression performance of arrays with differing numbers of elements can be compared. SINR loss is defined as

$$L_{\text{SINR}} = \frac{\text{SINR}}{\text{SNR}_\circ}, \tag{2.19}$$

where

$$\text{SNR}_\circ = \xi_t MNP \tag{2.20}$$

10

is the maximum output SNR limited only by noise, the number of pulses, and the number of array elements. SNR$_\circ$ is the optimum SNR achieved without interference.

2.2.3   Signal Match Power Spectra.   The signal match power estimator is discussed in [7]. It shows the interference due to the surrounding environment and the antenna pattern without adaptivity. Interference illuminated by the antenna pattern sidelobes shows up in the signal match power spectra. The normalized output power for the signal match method is

$$P = \frac{\mathbf{v}^H \mathbf{R} \mathbf{v}}{\mathbf{v}^H \mathbf{v}}. \tag{2.21}$$

The signal match method is a Fourier transform when element spacing is uniform.

2.2.4   Minimum Variance Estimator Power Spectra.   The other spectral estimation technique is a high resolution technique called the MVE [7]. The MVE algorithm decomposes the signal into single peaks and shows where the interference is physically located relative to the radar. Amplitude information under the MVE is meaningless because its high resolution capabilities introduce instabilities, causing a loss in amplitude estimation ability. Therefore, MVE simply tells you if a signal is present or not. The output power using the MVE method is

$$P = (\mathbf{v}^H \mathbf{R}^{-1} \mathbf{v})^{-1}. \tag{2.22}$$

2.3   STAP Methods

A few different STAP methods are examined for interference suppression capability. The matched filter and AMF attain the best possible performance, meaning they do the best job at suppressing interference. However, the matched filter and AMF are not practical because they require too much sample support. Reed [9] determined that twice the degrees of freedom (DOF) sample support vectors are required to obtain performance within 3 dB of optimal. Each practical STAP method uses reduced DOF to achieve performance comparable to the matched filter and AMF.

FTS and JDL are two practical STAP methods examined here since they are used for simulations in Chapters IV and V. The JDL and FTS algorithms are presented in [5] for uniformly spaced planar arrays and are updated in Chapter III to reflect the changes caused by non-uniform element spacing.

2.3.1 Matched Filter.   The matched filter, also called the optimum filter, can be found using the likelihood ratio, the maximum SINR, or the Wiener filter method [2]. The matched filter weights are found by projecting the space-time steering vector onto the covariance matrix inverse,

$$\mathbf{w} = \mathbf{R}^{-1}\mathbf{v}. \tag{2.23}$$

The matched filter is considered non-adaptive since the covariance matrix $\mathbf{R}$ of incoming space-time snapshots is known prior to receiving the incoming data. Detection probability is maximized by maximizing SINR using the matched filter.

2.3.2 Adaptive Matched Filter.   The AMF is similar to the matched filter, except the covariance matrix of incoming space-time snapshots is not known prior to receiving the data. Therefore, the covariance matrix is estimated from the data already received using the Maximum Likelihood Estimate (MLE) [9] and is represented as $\hat{\mathbf{R}}$. The AMF weights are

$$\hat{\mathbf{w}} = \hat{\mathbf{R}}^{-1}\mathbf{v}. \tag{2.24}$$

Incoming data must be estimated since it is constantly changing due to aircraft motion, heterogeneous clutter, jamming, etc. The AMF is fully adaptive because all DOF are used for covariance matrix estimation. Therefore, twice the number of array elements times the number of pulses in the coherent processing interval (CPI), or $2NMP$, sample support vectors are required to operate within 3 dB of optimal when using the AMF.

2.3.3 FTS. FTS is described in [5, 13] as an element-space post-Doppler method where the incoming signal from each antenna element is Doppler filtered first. The Doppler filtered data is then used to estimate the interference covariance matrix for spatially adaptive filtering. A window is typically applied across Doppler since FTS has no temporal degrees of freedom. Post-Doppler methods such as FTS intend to localize clutter in angle in order to reduce the adaptive degrees of freedom. FTS requires $2N$ sample support vectors to obtain performance within 3 dB of optimal when the array is linear. Two separate FTS algorithms are presented in [5], one for uniformly spaced linear arrays and one for uniformly spaced planar arrays. The FTS algorithm for uniform linear arrays is shown below since it is more similar to the FTS algorithm derived in Chapter III for non-uniformly spaced arrays. The Doppler filter bank is defined as

$$\mathbf{F} = \text{diag}(\mathbf{t_b})\mathbf{W}^H \tag{2.25}$$

where $\mathbf{W}$ is an $M \times M$ discrete Fourier transform (DFT) matrix. The Matlab® function "diag" creates a diagonal matrix from its vector argument $\mathbf{t_b}$, which can be a window function. Otherwise, $\mathbf{t_b}$ is simply a vector of ones. Equation (2.25) can be written as

$$\mathbf{F} = [\mathbf{f}_0 \quad \mathbf{f}_1 \quad \dots \quad \mathbf{f}_{M-1}] \tag{2.26}$$

showing each column of $\mathbf{F}$ represents a different Doppler filter. The FTS spatially adaptive filter weights for the mth Doppler bin are

$$\tilde{\mathbf{w}}_m = \tilde{\mathbf{R}}_m^{-1}\mathbf{a} \tag{2.27}$$

where

$$\tilde{\mathbf{R}}_m = (\mathbf{f}_m \otimes \mathbf{I}_N)^H \mathbf{R}(\mathbf{f}_m \otimes \mathbf{I}_N) \tag{2.28}$$

and $\mathbf{f}_m$ is the mth Doppler filter bin of $\mathbf{F}$.

13

2.3.4 JDL. The JDL algorithm is developed in [12] and presented in [5] for the uniformly spaced planar array. JDL is a beamspace post-Doppler method where adaptivity is applied after the incoming data is transformed from the space-time domain to the angle-Doppler domain. The spatial and temporal steering vectors are used to set up a localized processing region (LPR) using the transformation matrix

$$\mathbf{T} = [\mathbf{e}(\phi_t, \theta_{-1}) \ \ \mathbf{e}(\phi_t, \theta_0) \ \ \mathbf{e}(\phi_t, \theta_1)] \otimes [\mathbf{b}(\bar{\omega}_{-1}) \ \ \mathbf{b}(\bar{\omega}_0) \ \ \mathbf{b}(\bar{\omega}_1)]$$
$$\otimes [\mathbf{a}(\phi_{-1}, \theta_t) \ \ \mathbf{a}(\phi_0, \theta_t) \ \ \mathbf{a}(\phi_1, \theta_t)] \tag{2.29}$$

where θ_0, ϕ_0, and $\bar{\omega}_0$ are the elevation angle, azimuth angle, and Doppler frequency at the LPR center. The other angles and Doppler frequencies are simply the previous or next ones in the LPR. The LPR established by the transformation matrix in Eqn. (2.29) has 3 degrees of freedom in azimuth, 3 degrees of freedom in Doppler, and 3 degrees of freedom in elevation. The azimuth, Doppler, and elevation degrees of freedom are denoted η_a, η_b, and η_e, respectively. The transformation matrix is also used to transform the 3D steering vector,

$$\tilde{\mathbf{v}} = \mathbf{T}^H \mathbf{v}. \tag{2.30}$$

A reduced dimension estimated covariance matrix is also obtained from the transformation matrix as

$$\tilde{\mathbf{R}} = \mathbf{T}^H \mathbf{R} \mathbf{T}. \tag{2.31}$$

The filter weights are then computed and applied based on the transformed 3D steering vector and estimated covariance matrix

$$\begin{aligned} \tilde{\mathbf{w}} &= \tilde{\mathbf{R}}^{-1} \tilde{\mathbf{v}} \\ &= (\mathbf{T}^H \mathbf{R} \mathbf{T})^{-1} \mathbf{T}^H \mathbf{v}. \end{aligned} \tag{2.32}$$

JDL requires $2\eta_a\eta_b\eta_e$ sample support vectors to obtain performance within 3 dB of optimal.

2.4 *Previous Work With Circular Arrays*

STAP has typically been used with uniformly spaced arrays for radar systems in the past. Non-uniformly spaced arrays have recently been studied to determine if they possess any advantages over uniform arrays. There is a limited amount of information regarding STAP performance using non-uniformly spaced arrays in radar systems. The articles that are available mostly concentrate on circular arrays, particularly the circular array researched by the US Navy's Ultra-High Frequency (UHF) Electronically Scanned Array (UESA) program. A circular array can be electronically scanned across 360° in azimuth, whereas a uniform linear array must be mechanically steered to obtain the same coverage.

In two publications by Zatman [14, 15], the performance of STAP for airborne early warning (AEW) radar is evaluated when applied to the circular UESA. The circular array being simulated contains 60 elements. However, only 20 consecutive elements are active when transmitting and receiving. Therefore, the antenna can "rotate" in 6° increments based on the choice of excited elements and scans electronically ±3°. The 60 element sidelooking circular array is compared to an 18 element sidelooking uniform linear array. The two arrays have the same overall gain. A few other specific simulation parameters are presented in Table 2.1. However, the element spacing is not given. SINR loss is used as a performance metric to compare both arrays. Zatman's results show that SINR loss does not change as a function of range for the uniform linear array. The circular array has a wider clutter null, a higher clutter rank, and has about 0.5 dB more SINR loss than the uniform linear array. The performance of each array is also evaluated when there is a 30° array rotation. Array rotation is examined to study effects such as aircraft crab angle. In this case, the clutter null for the uniform linear array is broader than the clutter null for the circular array. Despite the wider clutter null, the uniform linear array SINR loss is

Table 2.1:   Simulation parameters in [14, 15] for 18 element uniform linear array and 60 element circular array.

Variable	Value
M	18
f_o	450 MHz
f_r	300 Hz
B	4 MHz
h_a (aircraft altitude)	9000 m
v_a (aircraft velocity)	100 knots
CNR	45 dB per element per pulse at 100 km
Transmit Taper	Uniform (None)

still about 0.5 dB higher than the circular array SINR loss. The simulations in [14,15] also evaluate pre-Doppler and post-Doppler STAP methods. It was found that post-Doppler STAP performs better than pre-Doppler STAP for the circular array since post-Doppler STAP reduces clutter rank through Doppler filtering. Range varying adaptive weights can be used to mitigate the range dependence of clutter caused by the circular array. The conclusions by Zatman are valuable since post-Doppler STAP methods are applied to circular arrays in Chapter V.

The previously established mathematical model for analyzing an airborne radar system with a sidelooking uniform array discussed in this chapter provides the basis for the model presented in the following chapter. Chapter III changes this airborne radar model to accommodate non-uniformly spaced arrays. A radar model for non-uniformly spaced arrays is valuable because any array configuration can be analyzed. An array can be evaluated to see how detection performance is affected when some of its elements fail to operate. Any array configuration can be simulated and compared to any other array using the model for non-uniform element spacing. This model is used in Chapter V to simulate circular arrays and uniform planar arrays with element failure.

III. Radar Model For Non-Uniform Element Spacing

This chapter incorporates non-uniform element spacing into the radar data model presented in [5]. Changing the element positions within the array affects the time/phase delay from element-to-element. This new time/phase delay causes the spatial steering vectors to change, bringing about changes in the array factor, the space-time snapshot $\boldsymbol{\chi}$, and covariance matrices. The model is valid for side-looking linear and planar arrays. The model can also accommodate 3-dimensional arrays. However, shadowing effects have not been taken into consideration. Shadowing occurs when the incoming radar wave does not strike some array elements due to their location. For example, this may occur in an array which conforms to the belly of an aircraft. In this case, the elements on the aircraft underside would not receive a signal coming in from above the aircraft. The development in this chapter parallels the development presented in [5] with the necessary changes.

3.1 Array Geometry

The non-uniformly spaced, side-looking array being modelled now contains N elements located in the xz-plane of the cartesian coordinate system. The radar platform's velocity vector is parallel to the positive x-axis shown in Fig. 3.1. Any element in the array can be defined as the reference element. The reference element can be located anywhere in the cartesian coordinate system in this development. An incoming radar echo strikes the reference element first and has a time delay associated with all other elements. The reference element should be logically chosen. For example, mathematical evaluation is less confusing when all elements are located in one quadrant of the coordinate system. In the uniform planar array situation, it makes sense to choose the upper left element as the reference element as in Fig. 3.1. The array elements can also be numbered in any order and the model will still be valid.

A new matrix containing the arbitrary element positions is defined as $\mathbf{D}$ which has three column vectors in it describing the x, y, and z positions of each element
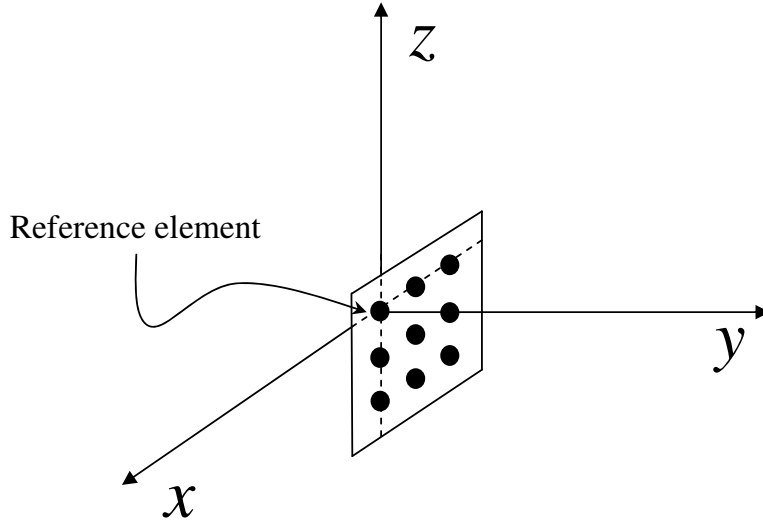
Figure 3.1:   Sidelooking planar array lying in the xz-plane. Boresight is defined as being parallel to the positive y-axis. The aircraft velocity vector is along the positive x-axis.

and is given by

$$\mathbf{D} = [\mathbf{d}_x \ \mathbf{d}_y \ \mathbf{d}_z]. \tag{3.1}$$

The nth row of $\mathbf{D}$ describes the nth element location and is written as $\mathbf{D}[n,:]$. Using the geometry of Fig. 3.1, the location of element n is

$$\mathbf{D}[n,:] = \mathbf{d}_x[n]\hat{\mathbf{x}} + \mathbf{d}_y[n]\hat{\mathbf{y}} + \mathbf{d}_z[n]\hat{\mathbf{z}}, \tag{3.2}$$

where $\mathbf{d}_x[n]$, $\mathbf{d}_y[n]$, and $\mathbf{d}_z[n]$ are scalar distances in meters measured from the nth element along the x-axis, y-axis, and z-axis, respectively, and $\hat{\mathbf{x}}$, $\hat{\mathbf{y}}$, and $\hat{\mathbf{z}}$ are unit vectors.

It is common to describe targets relative to the radar using a coordinate system other than the cartesian system. The radar coordinate system shown in Fig. 3.2 is similar to the spherical coordinate system. Elevation (θ) and azimuth (ϕ) angles are referenced to boresight in radar coordinates. Boresight is perpendicular to the array face and is along the positive y-axis in this development. Positive azimuth
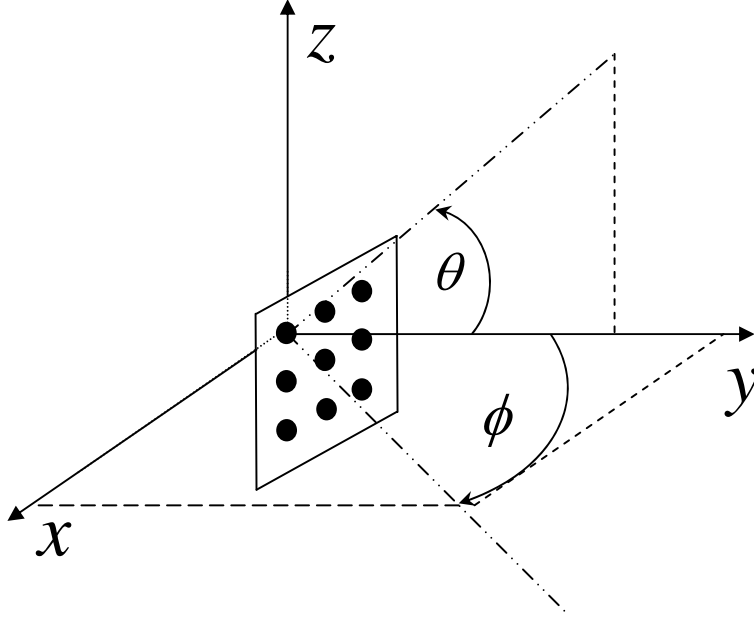
Figure 3.2:   Sidelooking planar array lying in the xz-plane. Negative elevation angle is measured from boresight towards the ground (negative z-axis). Positive elevation angle extends from boresight towards the sky (positive z-axis). Positive azimuth angle is measured from boresight towards the aircraft nose (positive x-axis). Negative azimuth angle extends from boresight towards the aircraft tail (negative x-axis).

angles are measured from boresight towards the aircraft nose, or the positive x-axis, while negative azimuth angles are measured from boresight towards the tail. Positive elevation angles are measured from boresight towards the sky, or the positive z-axis, while negative elevation angles are measured from boresight towards the ground. It is more insightful to mathematically analyze the radar model in the cartesian coordinate system since it is the most familiar coordinate system. Therefore, a transformation is necessary to convert an azimuth and elevation direction in the radar coordinate system to a direction in cartesian coordinates. This transformation is given in [13] as

$$\hat{\mathbf{k}}(\theta, \phi) = \cos\theta \sin\phi \hat{\mathbf{x}} + \cos\theta \cos\phi \hat{\mathbf{y}} + \sin\theta \hat{\mathbf{z}}. \tag{3.3}$$

A new element position matrix $\mathbf{D}$ is now set up to accommodate arbitrary array configurations. The element positions affect the received signal time/phase delay across the array. The transmit signal must be defined before the received signal can be described.

3.2 Transmit Signal

The signal transmitted from the radar is mathematically described in [13] as

$$\tilde{s}(t) = a_t u(t) e^{j(\omega_o t + \varphi)}, \tag{3.4}$$

where Eqn. (3.4) includes a random phase shift φ, a sinusoidal carrier frequency ω_o, a pulse amplitude a_t (assumed to have unity energy), and an envelope function $u(t)$. The pulse width and pulse repetition interval T_r are contained in the envelope function defined in [13] as

$$u(t) = \sum_{m=0}^{M-1} u_p(t - mT_r). \tag{3.5}$$

The summation of M pulses defines the CPI, which is a block of data available for radar processing. The radar uses this block of data to statistically model the environment. The antenna pattern is changed based on the CPI to null out interference and determine if a target is present. The received signal can now be determined since it is an echo response of the transmitted signal.

3.3 Received Signal

The signal received at the nth array element has the same form as the transmitted signal except that it is delayed in time by τ and shifted in frequency by f_t due to the target distance and velocity, respectively. The signal delay equals the round trip time to the target T_R plus the time it takes the signal to travel from the reference element across the array to the nth element τ_n'. The complete signal delay is

$$\tau_n = T_R + \tau_n'. \tag{3.6}$$

20

The signal received at the nth element is then written as

$$
\begin{aligned}
\tilde{s}_n &= \tilde{s}(t - \tau_n)e^{j2\pi f_t(t-\tau_n)} \\
&= a_r u(t - \tau_n)e^{j2\pi f_o(t-\tau_n)}e^{j2\pi f_t(t-\tau_n)}e^{j\varphi}.
\end{aligned} \tag{3.7}
$$

The received pulse amplitude a_r is different than the transmitted pulse amplitude a_t due to various factors such as the target's radar cross section (RCS) σ, atmospheric attenuation, system losses L_s, etc. as encapsulated in the radar equation of [10],

$$
R_{max}^4 = \frac{P_t G A_e \sigma}{(4\pi)^2 k T_o B F_n (S/N)_M L_s}. \tag{3.8}
$$

P_t is transmit power, G is transmit antenna gain, A_e is the effective received antenna aperture, k is Boltzmann's constant 1.38×10^{-23} J/deg, T_o is standard temperature 290 K, B is receiver bandwidth, F_n is receiver noise figure, and $(S/N)_M$ is the effective SNR of M integrated pulses.

The time delay from the reference element to the nth element is found by projecting the target direction unit vector onto a vector representing the nth element's location,

$$
\begin{aligned}
\tau_n' &= \frac{\hat{\mathbf{k}}(\theta, \phi) \cdot \mathbf{D}[n,:]}{c} \\
&= \frac{(\cos\theta\sin\phi\hat{\mathbf{x}} + \cos\theta\cos\phi\hat{\mathbf{y}} + \sin\theta\hat{\mathbf{z}}) \cdot (\mathbf{d}_x[n]\hat{\mathbf{x}} + \mathbf{d}_y[n]\hat{\mathbf{y}} + \mathbf{d}_z[n]\hat{\mathbf{z}})}{c} \\
&= \frac{\mathbf{d}_x[n]\cos\theta\sin\phi + \mathbf{d}_y[n]\cos\theta\cos\phi + \mathbf{d}_z[n]\sin\theta}{c}.
\end{aligned} \tag{3.9}
$$

Then, the phase delay to the nth element is simply the corresponding time delay multiplied by ω_o,

$$
\omega_o \tau_n' = 2\pi f_o \left(\frac{\mathbf{d}_x[n]\cos\theta\sin\phi + \mathbf{d}_y[n]\cos\theta\cos\phi + \mathbf{d}_z[n]\sin\theta}{c} \right). \tag{3.10}
$$

This phase delay can be rewritten in a simpler form by extending the spatial frequency definition of [5] to 3 dimensions as

$$
\begin{aligned}
\boldsymbol{\vartheta}[n] &= \frac{\hat{\mathbf{k}}(\theta, \phi) \cdot \mathbf{D}[n, :]}{\lambda_o} \\
&= \left(\frac{\mathbf{d}_x[n] \cos \theta \sin \phi + \mathbf{d}_y[n] \cos \theta \cos \phi + \mathbf{d}_z[n] \sin \theta}{\lambda_o} \right).
\end{aligned}
\tag{3.11}
$$

There are three separate spatial frequency components in Eqn. (3.11) for each array element, one for the x-axis, one for the y-axis, and one for the z-axis, represented as

$$
\boldsymbol{\vartheta}_x[n] = \frac{\mathbf{d}_x[n] \cos \theta \sin \phi}{\lambda_o},
\tag{3.12}
$$

$$
\boldsymbol{\vartheta}_y[n] = \frac{\mathbf{d}_y[n] \cos \theta \cos \phi}{\lambda_o},
\tag{3.13}
$$

and
$$
\boldsymbol{\vartheta}_z[n] = \frac{\mathbf{d}_z[n] \sin \theta}{\lambda_o}.
\tag{3.14}
$$

The spatial frequencies describe the received signal's expected delay to the nth element based on the target's location in space. Therefore, the spatial frequencies change based on the location of each element in the array. Using Eqns. (3.12) through (3.14), the phase delay to the nth element can be rewritten as

$$
\omega_o \tau'_n = 2\pi(\boldsymbol{\vartheta}_x[n] + \boldsymbol{\vartheta}_y[n] + \boldsymbol{\vartheta}_z[n]).
\tag{3.15}
$$

When Eqn. (3.6) is substituted into Eqn. (3.7), the received signal becomes

$$
\tilde{s}_n(t) = a_r u(t - T_R - \tau'_n) e^{j2\pi(f_o + f_t)(t - T_R - \tau'_n)} e^{j\varphi}.
\tag{3.16}
$$

A few assumptions can be made to reduce Eqn. (3.16). The first is the narrowband assumption: $\tau'_n \ll$ pulse width. In other words, the time delay from the reference element to the nth element can be neglected in the envelope function since it is much

smaller than the pulse width. Equation (3.16) now becomes

$$\tilde{s}_n(t) = a_r u(t - T_R)e^{j2\pi(f_o+f_t)t}e^{-j2\pi(f_o+f_t)T_R}e^{-j2\pi(f_o+f_t)\tau_n'}e^{j\varphi}. \tag{3.17}$$

The spatial frequencies of Eqns. (3.12) through (3.14) can be substituted into the third exponential term of the received signal

$$e^{-j2\pi f_o\tau_n'} = e^{-j\omega_o\tau_n'} = e^{-j2\pi(\vartheta_x[n]+\vartheta_y[n]+\vartheta_z[n])} \tag{3.18}$$

yielding

$$\tilde{s}_n(t) = a_r u(t - T_R)e^{j2\pi(f_o+f_t)t}e^{-j2\pi(f_o+f_t)T_R}e^{-j2\pi f_t\tau_n'}e^{-j2\pi(\vartheta_x[n]+\vartheta_y[n]+\vartheta_z[n])}e^{j\varphi}. \tag{3.19}$$

Examining the received signal again leads to another reduction. The second exponential term is constant, so it can be grouped into the arbitrary phase term $e^{j\varphi}$. The third exponential term can be approximated as 1 because the target Doppler shift f_t is assumed to be small relative to the carrier frequency f_o and the time delay τ_n' has the speed-of-light in its denominator. The received signal is now represented as

$$\tilde{s}_n(t) = a_r u(t - T_R)e^{j2\pi(f_o+f_t)t}e^{-j2\pi(\vartheta_x[n]+\vartheta_y[n]+\vartheta_z[n])}e^{j\varphi}. \tag{3.20}$$

After the signal is received, it is frequency down-converted by a mixer for processing. Figure 3.3 shows a simple block diagram of the receiver chain for one antenna element. The mixing process converts the signal frequency to an intermediate frequency (IF). In this derivation, the IF is assumed to be the baseband frequency. Therefore, the carrier frequency is no longer in the mixed signal

$$\tilde{s}_n(t) = a_r u(t - T_R)e^{j2\pi f_t t}e^{-j2\pi(\vartheta_x[n]+\vartheta_y[n]+\vartheta_z[n])}e^{j\varphi}. \tag{3.21}$$

After mixing, the received signal is match filtered to maximize echoes from the desired radar signal and to attenuate unwanted signals. The matched filter output is obtained
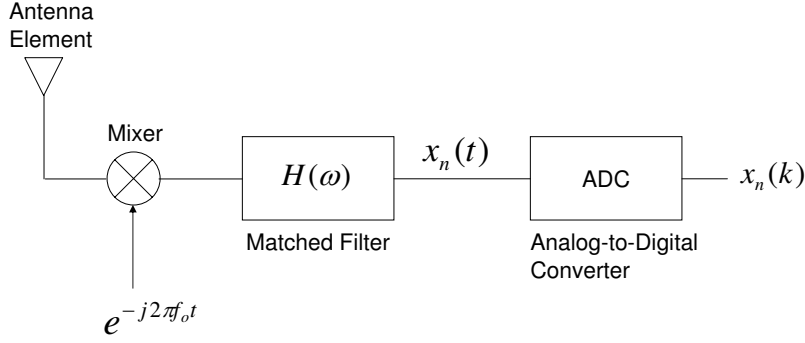
Figure 3.3: Basic block diagram of receiver for one antenna element. The signal is received by the antenna element. Then, the frequency is down converted to an intermediate frequency by a mixer. After mixing, the signal is match filtered. The signal is then sampled by an analog-to-digital converter for processing.

by convolving the filter impulse response with the received signal,

$$x_n(t) = \int_{-\infty}^{\infty} \tilde{s}_n(\delta) h(t - \delta) d\delta. \tag{3.22}$$

The filter impulse response is

$$h(t) = u_p^*(-t) \tag{3.23}$$

since the received signal is match filtered pulse-by-pulse. After substituting the received signal and filter impulse response into Eqn. (3.22), the matched filter output becomes

$$
\begin{aligned}
x_n(t) &= \int_{-\infty}^{\infty} a_r u(\delta - T_R) e^{j2\pi f_t \delta} e^{-j2\pi(\boldsymbol{\vartheta}_x[n] + \boldsymbol{\vartheta}_y[n] + \boldsymbol{\vartheta}_z[n])} e^{j\varphi} u_p^*(\delta - t) d\delta \tag{3.24} \\
&= a_r e^{-j2\pi(\boldsymbol{\vartheta}_x[n] + \boldsymbol{\vartheta}_y[n] + \boldsymbol{\vartheta}_z[n])} e^{j\varphi} \dots \\
&\quad \int_{-\infty}^{\infty} \sum_{m=0}^{M-1} u_p(\delta - T_R - mT_r) u_p^*(\delta - t) e^{j2\pi f_t \delta} d\delta. \tag{3.25}
\end{aligned}
$$

The matched filter output equation can be reduced by using a change of variables within the integral. Let $\beta = \delta - T_R - mT_r \Rightarrow \delta = \beta + T_R + mT_r$ and $d\beta/d\delta = 1$. Now

24

the matched filter output is

$$x_n(t) = a_r e^{-j2\pi(\boldsymbol{\vartheta}_x[n]+\boldsymbol{\vartheta}_y[n]+\boldsymbol{\vartheta}_z[n])} e^{j\varphi} e^{j2\pi f_t T_R} \sum_{m=0}^{M-1} e^{j2\pi f_t m T_r} \dots$$
$$\underbrace{\int_{-\infty}^{\infty} u_p(\beta) u_p^*(\beta + T_R + mT_r - t) e^{j2\pi f_t \beta} d\beta}_{\approx 1}. \qquad (3.26)$$

The integral term in Eqn. (3.26), known as the time frequency autocorrelation function (TFACF) for a transmitted pulse, can be approximated as 1 because the transmitted pulse was assumed to have unity energy and the mth pulse has a range delay of $T_R + mT_r$ at the range cell under test. This translates into a perfect match in range at the TFACF peak. The waveform is also assumed to be somewhat Doppler tolerant. Therefore, the match filtered signal for the array's n^{th} element and for a target at some range is

$$x_n = a_r e^{j\varphi} e^{-j2\pi(\boldsymbol{\vartheta}_x[n]+\boldsymbol{\vartheta}_y[n]+\boldsymbol{\vartheta}_z[n])} \sum_{m=0}^{M-1} e^{j2\pi m \bar{\omega}} \qquad (3.27)$$

where $\bar{\omega} = f_t/f_r$ is the normalized Doppler frequency and f_r is the pulse repetition frequency

$$f_r = 1/T_r. \qquad (3.28)$$

If the normalized Doppler frequency is greater than one, then the corresponding velocity is ambiguous to the radar. The $e^{j2\pi f_t T_R}$ term is lumped into the random phase term $e^{j\varphi}$ since it is constant. The mth match filtered pulse for the nth element can be expressed as

$$x_{nm} = \alpha_t e^{-j2\pi(\boldsymbol{\vartheta}_x[n]+\boldsymbol{\vartheta}_y[n]+\boldsymbol{\vartheta}_z[n])} e^{j2\pi m \bar{\omega}}, \qquad (3.29)$$

where α_t is a complex value representing the amplitude and random phase of the pulse. The match filtered signal is now in a form representing the response at each antenna element due to each pulse. From here, it is necessary to develop an expression representing the returns from all pulses across the entire array because the radar uses all the data within a CPI for target detection. First, the returns due to the nth element

25

and all M pulses can be written in an $M \times 1$ vector as

$$\mathbf{x}_n = \alpha_t e^{-j2\pi\boldsymbol{\vartheta}_x[n]} e^{-j2\pi\boldsymbol{\vartheta}_y[n]} e^{-j2\pi\boldsymbol{\vartheta}_z[n]} \mathbf{b}(\bar{\omega}) \qquad (3.30)$$

where

$$\mathbf{b}(\bar{\omega}) = [1 \quad e^{j2\pi\bar{\omega}} \quad ... \quad e^{j2\pi(M-1)\bar{\omega}}]^T \qquad (3.31)$$

is the temporal steering vector defined in [13]. Equation (3.30) is now a relaxed form of the incoming returns defined in [5] and accommodates arbitrary element spacing. At this point, there are a few different approaches that can be taken to represent the phase progression across all elements. One way is to write a column vector containing the phase progression to each element. Writing such a vector is the most direct method although it may be tedious for arrays with many elements. This vector of element phase progressions is called $\mathbf{c}$ and is written as

$$\begin{aligned}
\mathbf{c}(\theta, \phi) &= [e^{-j2\pi\boldsymbol{\vartheta}_x[0]} e^{-j2\pi\boldsymbol{\vartheta}_y[0]} e^{-j2\pi\boldsymbol{\vartheta}_z[0]} \quad e^{-j2\pi\boldsymbol{\vartheta}_x[1]} e^{-j2\pi\boldsymbol{\vartheta}_y[1]} e^{-j2\pi\boldsymbol{\vartheta}_z[1]} \quad ... \\
&\qquad e^{-j2\pi\boldsymbol{\vartheta}_x[N-1]} e^{-j2\pi\boldsymbol{\vartheta}_y[N-1]} e^{-j2\pi\boldsymbol{\vartheta}_z[N-1]}]^T.
\end{aligned} \qquad (3.32)$$

The Kronecker Product (see Appendix A) can then be taken with the $\mathbf{c}$ vector and the temporal steering vector to produce a vector known as the space-time snapshot $\boldsymbol{\chi}$. The space-time snapshot contains the returns from all elements and pulses and is

$$\boldsymbol{\chi}_t = \alpha_t \mathbf{b}(\bar{\omega}) \otimes \mathbf{c}(\theta, \phi) \qquad (3.33)$$

for a single point scatterer.

Expanding $\boldsymbol{\chi}_t$ results in

$$
\boldsymbol{\chi}_t = \alpha_t \begin{bmatrix} \begin{bmatrix} e^{-j2\pi\boldsymbol{\vartheta}_x[0]}e^{-j2\pi\boldsymbol{\vartheta}_y[0]}e^{-j2\pi\boldsymbol{\vartheta}_z[0]} \\ e^{-j2\pi\boldsymbol{\vartheta}_x[1]}e^{-j2\pi\boldsymbol{\vartheta}_y[1]}e^{-j2\pi\boldsymbol{\vartheta}_z[1]} \\ \vdots \\ e^{-j2\pi\boldsymbol{\vartheta}_x[N-1]}e^{-j2\pi\boldsymbol{\vartheta}_y[N-1]}e^{-j2\pi\boldsymbol{\vartheta}_z[N-1]} \end{bmatrix} \\ \begin{bmatrix} e^{j2\pi\bar{\omega}}e^{-j2\pi\boldsymbol{\vartheta}_x[0]}e^{-j2\pi\boldsymbol{\vartheta}_y[0]}e^{-j2\pi\boldsymbol{\vartheta}_z[0]} \\ e^{j2\pi\bar{\omega}}e^{-j2\pi\boldsymbol{\vartheta}_x[1]}e^{-j2\pi\boldsymbol{\vartheta}_y[1]}e^{-j2\pi\boldsymbol{\vartheta}_z[1]} \\ \vdots \\ e^{j2\pi\bar{\omega}}e^{-j2\pi\boldsymbol{\vartheta}_x[N-1]}e^{-j2\pi\boldsymbol{\vartheta}_y[N-1]}e^{-j2\pi\boldsymbol{\vartheta}_z[N-1]} \end{bmatrix} \\ \vdots \\ \begin{bmatrix} e^{j2\pi(M-1)\bar{\omega}}e^{-j2\pi\boldsymbol{\vartheta}_x[0]}e^{-j2\pi\boldsymbol{\vartheta}_y[0]}e^{-j2\pi\boldsymbol{\vartheta}_z[0]} \\ e^{j2\pi(M-1)\bar{\omega}}e^{-j2\pi\boldsymbol{\vartheta}_x[1]}e^{-j2\pi\boldsymbol{\vartheta}_y[1]}e^{-j2\pi\boldsymbol{\vartheta}_z[1]} \\ \vdots \\ e^{j2\pi(M-1)\bar{\omega}}e^{-j2\pi\boldsymbol{\vartheta}_x[N-1]}e^{-j2\pi\boldsymbol{\vartheta}_y[N-1]}e^{-j2\pi\boldsymbol{\vartheta}_z[N-1]} \end{bmatrix} \end{bmatrix} .
$$

The space-time snapshot contains the target amplitude and direction. The target spatial location is represented by the 3D steering vector

$$
\mathbf{v}(\bar{\omega}, \theta, \phi) = \mathbf{b}(\bar{\omega}) \otimes \mathbf{c}(\theta, \phi). \tag{3.34}
$$

The 3D steering vector describes the specific azimuth angle, elevation angle, and normalized Doppler frequency of a target at a particular location. The target return dependence on the 3D steering vector can now be seen when Eqn. (3.34) is substituted into Eqn. (3.33), resulting in

$$
\boldsymbol{\chi}_t = \alpha_t \mathbf{v}(\bar{\omega}, \theta, \phi). \tag{3.35}
$$

In other words, the space-time snapshot is simply the 3D steering vector scaled in amplitude and phase.

The 3D steering vector can be used to maximize the radar response in the radar "look direction." The complex conjugate of the 3D steering vector must be taken to

maximize the radar response. This complex conjugated steering vector can be thought of as the steering vector from the target to the radar, representing the expected phase delays across the array from a particular location in space. These expected phase delays are essentially *filter weights* for each element and pulse *allowing target returns to be constructively added*. The filter weight vector is

$$\mathbf{w} = \mathbf{v}(\bar{\omega}, \theta, \phi). \tag{3.36}$$

This particular weight vector is non-adaptive because it simply represents the expected phase delays from a target at a specific location in space without considering the interference from the surrounding environment. The filter weights are mathematically applied to the target returns by the inner product between the filter weight vector and the space-time snapshot, producing an output given by

$$
\begin{aligned}
\text{Output} \ &= \ \mathbf{w}^H \boldsymbol{\chi}_t = \mathbf{v}^H(\bar{\omega}, \theta, \phi) \boldsymbol{\chi}_t \\
&= \ \alpha_t \mathbf{v}^H(\bar{\omega}, \theta, \phi) \mathbf{v}(\bar{\omega}, \theta, \phi) \\
&= \ \alpha_t \sum_{n=0}^{N-1} \sum_{m=0}^{M-1} e^{j2\pi(\boldsymbol{\vartheta}_x[n]+\boldsymbol{\vartheta}_y[n]+\boldsymbol{\vartheta}_z[n])} e^{-j2\pi m\bar{\omega}} e^{-j2\pi(\boldsymbol{\vartheta}_x[n]+\boldsymbol{\vartheta}_y[n]+\boldsymbol{\vartheta}_z[n])} e^{j2\pi m\bar{\omega}} \\
&= \ \alpha_t MN. \tag{3.37}
\end{aligned}
$$

The multiplication and addition between the filter weights and the space-time snapshot represent coherent integration over M pulses across the entire array. The N factor in Eqn. (3.37) is the spatial coherent integration gain across the array, while M is the coherent integration gain from integrating M pulses.

The spatial steering vector is now defined for arbitrary element spacing, allowing the 3D steering vector and space-time snapshot for a scatterer to be determined. The spatial steering vector is used to determine the array pattern, jammer model, and clutter model. The array pattern is useful because it shows how the array illuminates the environment. The element pattern must be defined before the array pattern is discussed.

3.4   Element Pattern

Each element in the array is assumed to have identical voltage and power patterns as discussed in [6, 13]. The voltage pattern as defined for a planar array in [5] is

$$
f(\theta, \phi) = \begin{cases} \cos(\theta)\cos(\phi) & -90° \leq \phi, \theta \leq 90° \\ b_e \cos(\theta)\cos(\phi) & 90° \geq \phi, \theta \leq 270° \end{cases}
$$

where b_e is a backlobe scaling factor. Mutual coupling effects are not considered in this element pattern expression. The voltage pattern is described as a cosine pattern with backlobe attenuation and is shown in Fig. 3.4. The backlobe factor b_e models the attenuation resulting from the surfaces behind the antenna elements. Such surfaces may include the back of the array, the aircraft fuselage, or anything else behind the array that attenuates the transmitted signal. The element power pattern equals the
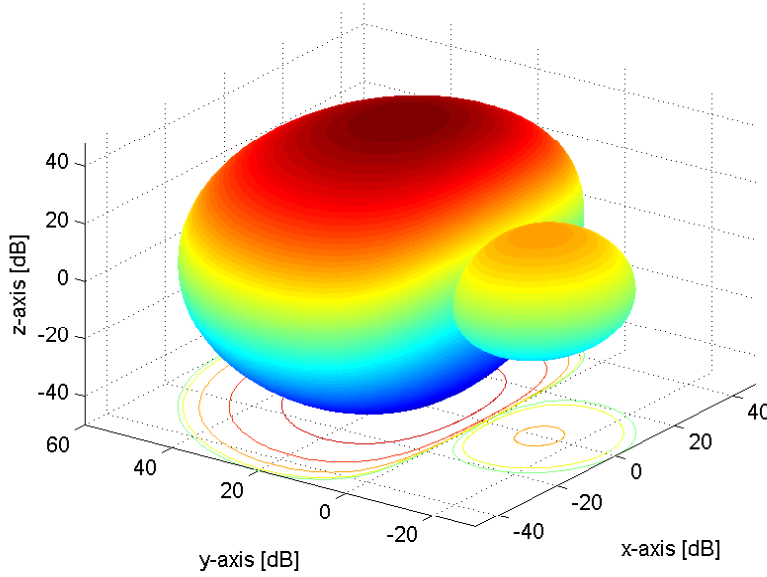

Figure 3.4:   3D element voltage pattern converted from radar coordinates to cartesian coordinates. This plot illustrates the energy emitted from each antenna element in a given direction. The antenna element is located at the origin ($x = 0$, $y = 0$, $z = 0$) for this illustration.

magnitude of the element voltage pattern squared

$$g(\theta, \phi) = |f(\theta, \phi)|^2. \tag{3.38}$$

The array pattern is defined in the next section since it is based on the element pattern.

3.5 Array Pattern

Once the voltage pattern is established for each element, the array pattern must be determined. The array pattern represents the overall transmitted voltage pattern from the entire array. Sidelobes, nulls, and backlobes are illustrated in the array pattern. The array pattern is constructed from the array factor and the element pattern. The array factor is the sum of all the phase weights across the array and is expressed as

$$W(\theta, \phi) = \mathbf{c}(\theta, \phi)^H \mathbf{c}(\theta', \phi'), \tag{3.39}$$

where vector $\mathbf{c}(\theta, \phi)$ contains the target location in space and vector $\mathbf{c}(\theta', \phi')$ contains the desired mainbeam location. Array beamforming theory is discussed more thoroughly in [1, 11]. The array factor is simply scaled by the element pattern to obtain the array pattern. The array voltage pattern is

$$F(\theta, \phi) = W(\theta, \phi) f(\theta, \phi) \tag{3.40}$$

and the array power pattern is

$$G(\theta, \phi) = |W(\theta, \phi) f(\theta, \phi)|^2 = |W(\theta, \phi)|^2 g(\theta, \phi). \tag{3.41}$$

A steerable antenna pattern can now be generated for an array with arbitrary element locations. The noise, jammer, and clutter models are described next because they are directly affected by the antenna pattern.

3.6 Interference Models

The next step in updating the radar data model is to reevaluate the interference models. Covariance matrices are used in the interference models to describe the statistical expectations of power across all elements and pulses at a specific range cell for a given source of interference. It is important to note that the noise, jammer, and clutter models are not actually being changed here. These models are simply being modified so interference can be modelled for non-uniformly spaced arrays.

3.6.1 Noise Model. Within the radar system, each array element has its own receiver. As a result, noise power is not correlated from element-to-element. Noise power is also uncorrelated from pulse-to-pulse since it is assumed to be white noise. This assumption is only applicable when the PRF is much less than the waveform bandwidth and the waveform bandwidth is much less than the carrier frequency. The resulting expected noise power for any given element and pulse is very similar to the expected value of any other element and pulse. Therefore, the noise covariance matrix established in [13] is the noise power per element per pulse σ^2 multiplied by an identity matrix of size MN

$$\mathbf{R}_n = \varepsilon\{\boldsymbol{\chi}_n\boldsymbol{\chi}_n^H\} = \sigma^2\mathbf{I}_{MN}. \tag{3.42}$$

! The noise covariance matrix in [13] is for a linear array containing N elements. The noise covariance matrix in Eqn. (3.42) is for a linear, planar, or 3D array with N total elements.

It can be seen from Eqn. (3.42) that the noise covariance matrix only depends on the number of elements and pulses. Element position on the array does not affect the expected noise power. Therefore, the noise covariance matrix is identical for arrays with the same number of elements despite the element positions.

3.6.2 Barrage Noise Jammer Model. The jammer model is for a barrage noise jammer [5,6,13]. Although it is not used in simulations in the following chapters,

the jammer model is presented here for completeness. Its power spectral density received at any element is

$$J_o = \frac{S_j g(\theta, \phi) \lambda_o^2}{(4\pi)^2 R_j^2 L_r}. \tag{3.43}$$

L_r is receiver losses, R_j is the distance between the radar and jammer, and S_j is the jammer's effective transmitted power spectral density. The expected jammer power is spatially correlated since the jammer is located at a specific elevation angle and azimuth angle. However, there is no temporal correlation because the transmitted jammer amplitude is complex and varies from pulse-to-pulse. The random jammer amplitudes are written in vector form as

$$\boldsymbol{\alpha}_j = [\alpha_0 \ \ \alpha_1 \ \ ... \ \ \alpha_{M-1}]^T. \tag{3.44}$$

The size of this vector is $M \times 1$ since there is a different amplitude for each pulse. The space-time snapshot for the barrage noise jammer is expressed as

$$\boldsymbol{\chi}_j = \boldsymbol{\alpha}_j \otimes \mathbf{c}(\theta, \phi). \tag{3.45}$$

The jammer covariance matrix can be found from the space-time snapshot as

$$\mathbf{R}_j = \varepsilon\{\boldsymbol{\chi}_j \boldsymbol{\chi}_j^H\} = \varepsilon\{[\boldsymbol{\alpha}_j \otimes \mathbf{c}(\theta, \phi)][\boldsymbol{\alpha}_j \otimes \mathbf{c}(\theta, \phi)]^H\}. \tag{3.46}$$

If the transmitted jammer power is assumed to be stationary over a CPI, then

$$\varepsilon\{\boldsymbol{\alpha}_j \boldsymbol{\alpha}_j^H\} = \sigma^2 \xi_j \mathbf{I}_M, \tag{3.47}$$

where

$$\xi_j = \frac{J_o}{N_o} \tag{3.48}$$

is the jammer-to-noise ratio per element. This assumption reduces the jammer covariance matrix to

$$\mathbf{R}_j = \sigma^2 \xi_j \mathbf{I}_M \otimes \mathbf{c}(\theta, \phi) \mathbf{c}(\theta, \phi)^H. \tag{3.49}$$

3.6.3   Clutter Model.   The clutter covariance matrix describes the natural environment surrounding the platform. Radar signals bounce off trees, buildings, and other objects in the environment. The clutter model used is a constant gamma model [10] for ground or sea clutter. Sky clutter is neglected in this model because it is so small compared to ground clutter. A few different distances and angles defined in [5] are reiterated here for the clutter model development. The earth is considered to be a perfect sphere with an effective radius 4/3 its normal size, $a_e = 4r_e/3$. Clutter is divided into rings and patches around the aircraft as in Fig. 3.5. Each clutter ring surrounds the aircraft at a range R_c. The elevation angle from the aircraft to the clutter ring is

$$\theta_c = -\sin^{-1}\left[\frac{R_c^2 + h_a(h_a + 2a_e)}{2R_c(a_e + h_a)}\right],\qquad(3.50)$$

where h_a is the aircraft altitude. Each clutter ring is divided into N_c patches. The
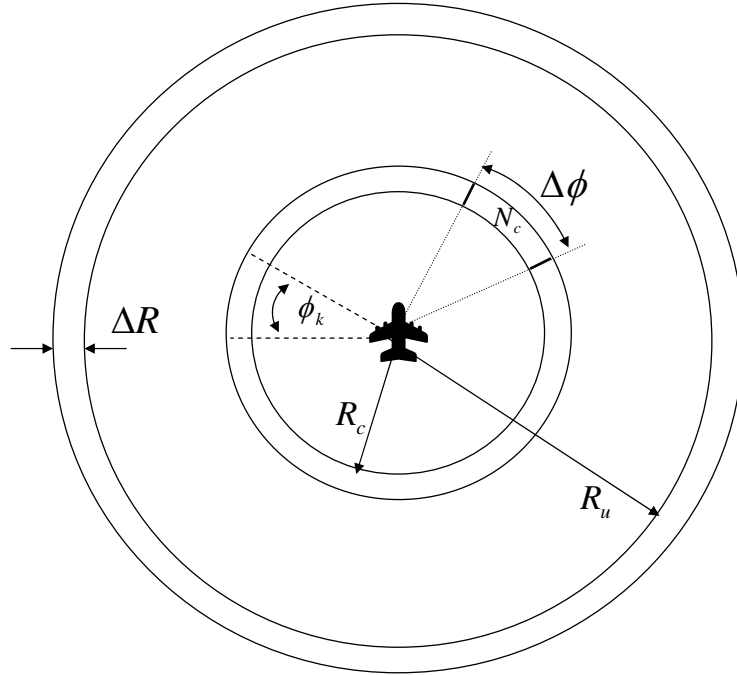
Figure 3.5:   Overhead view of clutter rings and patches surrounding the radar platform.

33

grazing angle ψ_c shown in Fig. 3.6 is defined as the angle between a line tangent to the earth at the clutter patch and a line from the radar to the clutter patch. The grazing angle is determined as

$$\psi_c = -\sin^{-1}\left[\frac{R_c^2 - h_a(h_a + 2a_e)}{2R_c a_e}\right].$$ (3.51)

The grazing angle is set equal to 0 to determine the range from the aircraft to the horizon. The horizon range is

$$R_h = \sqrt{h_a^2 + 2h_a a_e}.$$ (3.52)

The unambiguous range $R_u = cT_r/2$ is used with the horizon range to determine the number of range ambiguities N_r as

$$N_r = \begin{cases} \left\lceil \frac{R_h}{R_u} \right\rceil & R_c N_r \le R_h \\[2ex] \left\lfloor \frac{R_h}{R_u} \right\rfloor & R_c N_r > R_h, \end{cases}$$

where $\lceil x \rceil$ means round up to the nearest integer and $\lfloor x \rfloor$ means round down to

Figure 3.6:   Side view of clutter ring layout, showing the grazing angle.

the nearest integer. The ambiguous range rings are at $R_i = iR_u + R_c$ where $i = 0, 1, ..., N_r - 1$.

The major change that takes place in the clutter model for non-uniform element spacing is the spatial frequency of the ik^{th} clutter patch, where the i subscript defines the current clutter ring based on elevation angle θ_i and the k subscript designates the current pat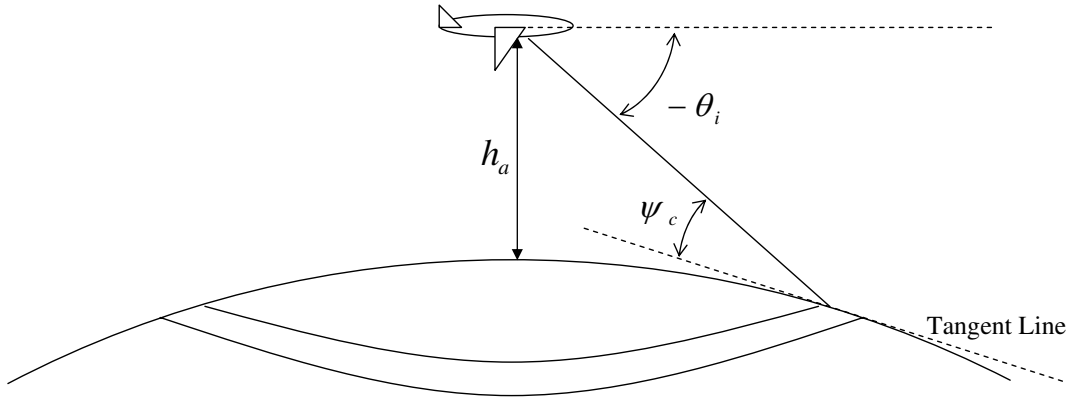ch around the clutter ring based on azimuth angle ϕ_k. The vector describing the elevation and azimuth angle of the ik^{th} clutter patch is projected onto the array's n^{th} element and divided by the wavelength. The spatial frequency defined in Eqn. (3.11) is evaluated at θ_i and ϕ_k

$$
\begin{aligned}
\boldsymbol{\vartheta}_{ik}[n] &= \frac{\hat{\mathbf{k}}(\theta_i, \phi_k) \cdot \mathbf{D}[n, :]}{\lambda_o} \\
&= \frac{\mathbf{d}_x[n] \cos \theta_i \sin \phi_k + \mathbf{d}_y[n] \cos \theta_i \cos \phi_k + \mathbf{d}_z[n] \sin \theta_i}{\lambda_o}
\end{aligned}
\tag{3.53}
$$

for the ik^{th} clutter patch. The Doppler frequency of the ik^{th} clutter patch must also be determined in order to construct the clutter space-time snapshot. Using Eqn. (3.3), the ik^{th} clutter patch Doppler frequency is defined as

$$
\begin{aligned}
f_c(\theta_i, \phi_k) &= \frac{2\hat{\mathbf{k}}(\theta_i, \phi_k) \cdot \mathbf{v}_a}{\lambda_o} \\
&= \frac{2v_a \cos \theta_i \sin \phi_k}{\lambda_o},
\end{aligned}
\tag{3.54}
$$

where $\mathbf{v}_a = v_a \hat{\mathbf{x}}$ is the aircraft velocity vector. The clutter space-time snapshot is determined as

$$
\boldsymbol{\chi}_c = \sum_{i=0}^{N_r - 1} \sum_{k=0}^{N_c - 1} \alpha_{ik} \mathbf{b}(\bar{\omega}_{ik}) \otimes \mathbf{c}(\theta_i, \phi_k),
\tag{3.55}
$$

using the normalized Doppler frequency $\bar{\omega}_{ik}$, elevation angle θ_i, and azimuth angle ϕ_k of the ik^{th} clutter patch. The summations in Eqn. (3.55) physically represent the sum of all returns from each clutter patch around each range ring. The random clutter

35

patch amplitude α_{ik} is found based on its RCS. The ik^{th} clutter patch's RCS is

$$\sigma_{ik} = \sigma_0(\theta_i, \phi_k) R_i \Delta\phi\Delta R \sec(\psi_i), \tag{3.56}$$

where $\Delta\phi = (2\pi/N_c)$ and $\Delta R = c/(2B)$. The radar system bandwidth is B. Each clutter patch is assumed to have a specific backscatter reflectivity described by

$$\sigma_0(\theta_i, \phi_k) = \gamma \sin\psi_i, \tag{3.57}$$

where ψ_i is the grazing angle. The γ term characterizes clutter. A worst case clutter environment may have a γ value as high as -3 dB, suggesting the clutter is very strong and may be caused by an urban environment [8]. Clutter can be as weak as -29 dB, indicating flat terrain such as a desert environment [8]. After the clutter patch RCS is determined, the element clutter-to-noise ratio (CNR) can be calculated as

$$\xi_{ik} = \frac{P_t G_t(\theta_i, \phi_k) g(\theta_i, \phi_k) \lambda_o^2 \sigma_{ik}}{(4\pi)^3 N_o B L_s R_i^4} \tag{3.58}$$

using the radar equation. The clutter patch amplitude is found by simply multiplying the CNR by the noise power σ^2.

Once the clutter patch amplitude is found, the clutter space-time snapshot can be computed using Eqn. (3.55). Then, the clutter covariance matrix is found by taking the expected value of the space-time snapshot's outer product

$$\mathbf{R}_c = \varepsilon\{\boldsymbol{\chi}_c\boldsymbol{\chi}_c^H\} = \sigma^2 \sum_{i=0}^{N_r-1} \sum_{k=0}^{N_c-1} \xi_{ik}\mathbf{b}(\bar{\omega}_{ik})\mathbf{b}(\bar{\omega}_{ik})^H \otimes \mathbf{c}(\theta_i, \phi_k)\mathbf{c}(\theta_i, \phi_k)^H. \tag{3.59}$$

The radar model is now in a format suitable for radar system modelling and analysis of non-uniformly spaced arrays. Antenna patterns can be generated and interference can be modelled. The next logical step is to update the STAP models so STAP can be applied to non-uniform arrays.

3.7 STAP Models

Two practical STAP algorithms, JDL and FTS, are updated in this section. The MF and AMF algorithms discussed in Chapter II do not need to be modified because the 3D steering vector $\mathbf{v}$ accounts for the non-uniform spacing.

3.7.1 Joint Domain Localized. The JDL model changes based on the spatial steering vector $\mathbf{c}(\theta, \phi)$. The incoming space-time snapshot data is transformed to the angle-Doppler domain using the redefined transformation matrix

$$\mathbf{T} = [\mathbf{b}(\bar{\omega}_{-1})\quad \mathbf{b}(\bar{\omega}_0)\quad \mathbf{b}(\bar{\omega}_1)] \otimes [\mathbf{c}(\theta_{-1}, \phi_{-1})\quad \mathbf{c}(\theta_{-1}, \phi_0)\quad \mathbf{c}(\theta_{-1}, \phi_1)$$
$$\mathbf{c}(\theta_0, \phi_{-1})\quad \mathbf{c}(\theta_0, \phi_0)\quad \mathbf{c}(\theta_0, \phi_1)\quad \mathbf{c}(\theta_1, \phi_{-1})\quad \mathbf{c}(\theta_1, \phi_0)\quad \mathbf{c}(\theta_1, \phi_1)]. \tag{3.60}$$

The spatial steering vector $\mathbf{c}(\theta, \phi)$ in Eqn. (3.60) contains the phase progression to each element based on the azimuth and elevation angle of interest, ϕ_0 and θ_0. The resulting transformation matrix is of size $NM \times \eta_b \eta_a \eta_e$ where η_b, η_a, and η_e are the degrees of freedom in Doppler, azimuth, and elevation, respectively. $\mathbf{T}$ in Eqn. (3.60) has $3 \times 3 \times 3$ degrees of freedom since there are 3 different Doppler values, 3 different azimuth angles, and 3 different elevation angles. This $3 \times 3 \times 3$ region contained within the entire angle-Doppler space is known as the localized processing region (LPR). Once the transformation matrix has been updated, the rest of the JDL algorithm is identical to the one presented in [5] and discussed in Chapter II. The transformed space-time snapshot and steering vector are still $\tilde{\boldsymbol{\chi}} = \mathbf{T}^H \boldsymbol{\chi}$ and $\tilde{\mathbf{v}} = \mathbf{T}^H \mathbf{v}$, respectively. The estimated covariance matrix is $\tilde{\mathbf{R}} = \varepsilon\{\tilde{\boldsymbol{\chi}}\tilde{\boldsymbol{\chi}}^H\} = \mathbf{T}^H \mathbf{R} \mathbf{T}$. The adaptive filter is $\tilde{\mathbf{w}} = \tilde{\mathbf{R}}^{-1}\tilde{\mathbf{v}}$.

3.7.2 Factored Time-Space. The FTS algorithm in [5, 13] also has a slight modification based on the new radar model for non-uniform element spacing. The Doppler filter bank is the same as in [5],

$$\mathbf{F} = \mathrm{diag}(\mathbf{t_b})\mathbf{W}^H. \tag{3.61}$$

The "diag" term is a Matlab® function that creates a diagonal matrix from the vector argument and $\mathbf{W}^H$ is an $M \times M$ DFT matrix. The $\mathbf{t_b}$ term can either be a vector of ones or a window function. If $\mathbf{t_b}$ is a vector of ones, then each column of $\mathbf{F}$ is simply the temporal steering vector $\mathbf{b}(\bar{\omega})$ for a different Doppler frequency. Equation (3.61) can be expanded as

$$\mathbf{F} = [\mathbf{f}_0 \quad \mathbf{f}_1 \quad \ldots \quad \mathbf{f}_{M-1}], \tag{3.62}$$

showing each column as the Doppler filter for each bin. The output from Doppler bin m is

$$\tilde{\boldsymbol{\chi}}_m = (\mathbf{f}_m \otimes \mathbf{I}_N)^H \boldsymbol{\chi} \tag{3.63}$$

when applied to the space-time snapshot. The spatially adaptive filter weights for the mth Doppler bin are

$$\tilde{\mathbf{w}}_m = \tilde{\mathbf{R}}_m^{-1} \mathbf{c}(\theta, \phi), \tag{3.64}$$

where the covariance matrix

$$\tilde{\mathbf{R}}_m = \varepsilon\{\tilde{\boldsymbol{\chi}}_m \tilde{\boldsymbol{\chi}}_m^H\} = (\mathbf{f}_m \otimes \mathbf{I}_N)^H \mathbf{R} (\mathbf{f}_m \otimes \mathbf{I}_N) \tag{3.65}$$

is now of size $N \times N$, reducing the required sample support. The rest of the FTS algorithm is the same as [5]. For example, the full dimensioned weight vector is

$$\mathbf{w}_m = \mathbf{f}_m \otimes \tilde{\mathbf{w}}_m. \tag{3.66}$$

3.8   Summary

The radar model has been updated to incorporate non-uniform element spacing for linear and planar arrays. The changes began by redefining the position vector describing each element location in the array. The new element position definition affects the propagating wave time/phase delay across the array, the spatial frequencies, the steering vectors, the array pattern, the space-time snapshots, and the covariance matrices. The JDL and FTS STAP algorithms have also been modified so they are

compatible with the new airborne radar model for non-uniform element spacing. The model is in a format suitable for data generation and analysis.

IV. Radar Model Verification

The new radar model derived in Chapter III for non-uniform element spacing is verified in this chapter. Verification is accomplished by inserting uniform element spacing into the model derived for non-uniform element spacing. Then, the radar model presented in Chapter III is compared to the models in [13] and [5] to see if they produce the same results. The model presented in Chapter III will identically collapse back to the model in [5, 13] only when the array is linear. The two models still produce the same results when the array is planar, except the steering vectors, the space-time snapshots, and the covariance matrices are ordered differently in each model. Therefore, Matlab® simulation is used to verify that the model in Chapter III produces the same results as the model in [5] when the planar array contains uniform element spacing.

4.1 Linear Array

The model presented in [5] is for a planar array with N azimuth channels and P elevation channels. When $P = 1$, the array contains N elements extending along the negative x-axis with the reference element located at the origin, as in [13]. The inter-element spacing between each element is d_x. The position vector of each element defined in Chapter III as

$$\mathbf{D}[0,:] = \mathbf{d}_x[0]\hat{\mathbf{x}} + \mathbf{d}_y[0]\hat{\mathbf{y}} + \mathbf{d}_z[0]\hat{\mathbf{z}}$$
$$\mathbf{D}[1,:] = \mathbf{d}_x[1]\hat{\mathbf{x}} + \mathbf{d}_y[1]\hat{\mathbf{y}} + \mathbf{d}_z[1]\hat{\mathbf{z}}$$
$$\vdots$$
$$\mathbf{D}[N-2,:] = \mathbf{d}_x[N-2]\hat{\mathbf{x}} + \mathbf{d}_y[N-2]\hat{\mathbf{y}} + \mathbf{d}_z[N-2]\hat{\mathbf{z}}$$
$$\mathbf{D}[N-1,:] = \mathbf{d}_x[N-1]\hat{\mathbf{x}} + \mathbf{d}_y[N-1]\hat{\mathbf{y}} + \mathbf{d}_z[N-1]\hat{\mathbf{z}}$$

can now be written as

$$\mathbf{D}[0,:] = -(0)d_x\hat{\mathbf{x}} + (0)\hat{\mathbf{y}} + (0)\hat{\mathbf{z}}$$
$$\mathbf{D}[1,:] = -(1)d_x\hat{\mathbf{x}} + (0)\hat{\mathbf{y}} + (0)\hat{\mathbf{z}}$$
$$\vdots$$
$$\mathbf{D}[N-2,:] = -(N-2)d_x\hat{\mathbf{x}} + (0)\hat{\mathbf{y}} + (0)\hat{\mathbf{z}}$$
$$\mathbf{D}[N-1,:] = -(N-1)d_x\hat{\mathbf{x}} + (0)\hat{\mathbf{y}} + (0)\hat{\mathbf{z}}$$

due to uniform element spacing. By examining the above element position vectors, the nth element location can be expressed as

$$\begin{aligned}\mathbf{D}[n,:] &= -(n)d_x\hat{\mathbf{x}} + 0\hat{\mathbf{y}} + 0\hat{\mathbf{z}} \\ &= -nd_x\hat{\mathbf{x}}.\end{aligned} \tag{4.1}$$

The $\hat{\mathbf{y}}$ and $\hat{\mathbf{z}}$ terms are neglected since the linear array is located along the x-axis at $d_y = d_z = 0$. The position vector is consistent with [5] for a linear array and flows through the entire radar model. For example, the spatial frequency becomes

$$\begin{aligned}\boldsymbol{\vartheta}[n] &= \frac{\hat{\mathbf{k}}(\theta,\phi) \cdot \mathbf{D}[n,:]}{\lambda_o} \\ &= \frac{\mathbf{d}_x[n]\cos\theta\sin\phi}{\lambda_o} \\ &= \frac{-nd_x\cos\theta\sin\phi}{\lambda_o}.\end{aligned} \tag{4.2}$$

The spatial frequency x-component is defined in [13] as a scalar

$$\vartheta_x = \frac{d_x\cos\theta\sin\phi}{\lambda_o}, \tag{4.3}$$

41

so that $\boldsymbol{\vartheta}[n] = -n\vartheta_x$. Now, Eqn. (4.3) is consistent with the spatial frequency component in [5]. Then, the nth phase delay is

$$
\begin{aligned}
\omega_o \tau_n' &= 2\pi \boldsymbol{\vartheta}[n] \\
&= -2\pi(n\vartheta_x).
\end{aligned}
\tag{4.4}
$$

Proceeding through the radar model framework shows that the return from the mth pulse at the nth element is

$$
\begin{aligned}
x_{nm} &= \alpha_t e^{-j2\pi\boldsymbol{\vartheta}[n]} e^{j2\pi m\bar{\omega}} \\
&= \alpha_t e^{j2\pi(n\vartheta_x)} e^{j2\pi m\bar{\omega}}.
\end{aligned}
\tag{4.5}
$$

The spatial steering vector $\mathbf{c}(\theta, \phi)$ must also be verified using uniform element spacing. Inserting uniform element spacing into $\mathbf{c}(\theta, \phi)$ gives

$$
\begin{aligned}
\mathbf{c}(\theta, \phi) &= \begin{bmatrix} e^{-j2\pi\boldsymbol{\vartheta}[0]} & e^{-j2\pi\boldsymbol{\vartheta}[1]} & \dots & e^{-j2\pi\boldsymbol{\vartheta}[N-1]} \end{bmatrix}^T \\
&= \begin{bmatrix} e^{j2\pi(0)\vartheta_x} & e^{j2\pi(1)\vartheta_x} & \cdots & e^{j2\pi(N-1)\vartheta_x} \end{bmatrix}^T.
\end{aligned}
\tag{4.6}
$$

Equation (4.6) is equivalent to the azimuth spatial steering vector $\mathbf{a}(\vartheta_x)$ defined in [5]. Changing $\mathbf{c}(\theta, \phi)$ to $\mathbf{a}(\vartheta_x)$ brings about many changes that ripple through the radar model. The 3D steering vector defined in Chapter III as $\mathbf{v}(\bar{\omega}, \theta, \phi) = \mathbf{b}(\bar{\omega}) \otimes \mathbf{c}(\theta, \phi)$ can now be written as

$$
\mathbf{v}(\bar{\omega}, \phi) = \mathbf{b}(\bar{\omega}) \otimes \mathbf{a}(\vartheta_x).
\tag{4.7}
$$

The 3D steering vector defined in [5] is

$$
\mathbf{v}(\bar{\omega}, \theta, \phi) = \mathbf{e}(\vartheta_z) \otimes \mathbf{b}(\bar{\omega}) \otimes \mathbf{a}(\vartheta_x)
\tag{4.8}
$$

where the elevation steering vector is

$$
\mathbf{e}(\vartheta_z) = \begin{bmatrix} 1 & e^{j2\pi\vartheta_z} & \dots & e^{j2\pi(P-1)\vartheta_z} \end{bmatrix}.
\tag{4.9}
$$

The elevation steering vector becomes $\mathbf{e}(\vartheta_z)=1$ when $P = 1$. Therefore, Eqn. (4.8) reduces to Eqn. (4.7) when the uniformly spaced array is linear. The space-time snapshot $\boldsymbol{\chi}_t$ has the exact same change as the 3D steering vector since the 3D steering vector is contained within the space-time snapshot.

The next major change to be verified is the array factor previously defined as $W(\theta, \phi) = \mathbf{c}(\theta, \phi)^H \mathbf{c}(\theta', \phi')$. The array factor now becomes $W(\phi) = \mathbf{a}(\vartheta_x)^H \mathbf{a}(\vartheta'_x)$. The array factor defined in [5]

$$W(\theta, \phi) = [\mathbf{e}(\vartheta_z) \otimes \mathbf{a}(\vartheta_x)]^H \mathbf{1} \tag{4.10}$$

is for a mainbeam at boresight. Equation (4.10) is equivalent to

$$W(\theta, \phi) = [\mathbf{e}(\vartheta_z) \otimes \mathbf{a}(\vartheta_x)]^H [\mathbf{e}(\vartheta'_z) \otimes \mathbf{a}(\vartheta'_x)] \tag{4.11}$$

when the mainbeam is at boresight. Equation (4.11) simply allows the mainbeam to be steered anywhere and becomes

$$W(\phi) = \mathbf{a}(\vartheta_x)^H \mathbf{a}(\vartheta'_x) \tag{4.12}$$

when the array is linear. The equality of Eqns. (4.10) and (4.11) is demonstrated by inserting $\phi = 0$ and $\theta = 0$ into ϑ'_x and ϑ'_z, yielding

$$\vartheta'_x = \frac{d_x \cos(0) \sin(0)}{\lambda_o} = 0$$

and

$$\vartheta'_z = \frac{d_z \sin(0)}{\lambda_o} = 0.$$

Then, the elevation steering vector becomes

$$
\begin{aligned}
\mathbf{e}(\vartheta_z') &= \begin{bmatrix} 1 & e^{j2\pi\vartheta_z'} & \dots & e^{j2\pi(P-1)\vartheta_z'} \end{bmatrix} \\
&= \begin{bmatrix} 1 & e^{j2\pi(0)} & \dots & e^{j2\pi(P-1)(0)} \end{bmatrix} \\
&= \begin{bmatrix} 1 & 1 & \dots & 1 \end{bmatrix}
\end{aligned}
\tag{4.13}
$$

and the azimuth steering vector becomes

$$
\begin{aligned}
\mathbf{a}(\vartheta_x') &= \begin{bmatrix} 1 & e^{j2\pi\vartheta_x'} & \dots & e^{j2\pi(N-1)\vartheta_x'} \end{bmatrix} \\
&= \begin{bmatrix} 1 & e^{j2\pi(0)} & \dots & e^{j2\pi(N-1)(0)} \end{bmatrix} \\
&= \begin{bmatrix} 1 & 1 & \dots & 1 \end{bmatrix}.
\end{aligned}
\tag{4.14}
$$

Since the element pattern does not change between each radar model and the array factors were just shown to be identical when the array is linear, the antenna array pattern is also equivalent between the two models.

The jammer and clutter models are the final portion of the radar model to be verified. The noise model is identical for both uniform and non-uniform element spacing as described in Chapter III. The barrage noise jammer space-time snapshot $\boldsymbol{\chi}_j = \boldsymbol{\alpha}_j \otimes \mathbf{c}(\theta, \phi)$ is now

$$
\boldsymbol{\chi}_j = \boldsymbol{\alpha}_j \otimes \mathbf{a}(\vartheta_x).
\tag{4.15}
$$

The barrage noise jammer space-time snapshot for uniform element spacing $\boldsymbol{\chi}_j = \mathbf{e}(\vartheta_z) \otimes \boldsymbol{\alpha}_j \otimes \mathbf{a}(\vartheta_x)$ reduces to Eqn. (4.15) when the array is linear. The jammer covariance matrix changes to

$$
\mathbf{R}_j = \sigma^2 \xi_j \mathbf{I}_M \otimes \mathbf{a}(\vartheta_x) \mathbf{a}^H(\vartheta_x)
\tag{4.16}
$$

based on the change in $\boldsymbol{\chi}_j$. This jammer covariance matrix is equivalent to the one defined in [13].

44

The change in the clutter model begins with the ik^{th} clutter patch spatial frequency,

$$
\begin{aligned}
\boldsymbol{\vartheta}_{ik}[n] &= \frac{\hat{\mathbf{k}}(\theta_i, \phi_k) \cdot \mathbf{D}[n, :]}{\lambda_o} \\
&= \frac{\mathbf{d}_x[n] \cos \theta_i \sin \phi_k}{\lambda_o} \\
&= \frac{-n d_x \cos \theta_i \sin \phi_k}{\lambda_o}.
\end{aligned}
\tag{4.17}
$$

The spatial frequency definition of Eqn. (4.3) can be substituted into Eqn. (4.17) to give $\boldsymbol{\vartheta}_{ik}[n] = -n\vartheta_x$. The azimuth steering vector $\mathbf{a}(\vartheta_x)$ can be substituted for $\mathbf{c}(\theta_i, \phi_k)$ in the clutter space-time snapshot defined in Chapter III to give

$$
\boldsymbol{\chi}_c = \sum_{i=0}^{N_r-1} \sum_{k=0}^{N_c-1} \alpha_{ik} \mathbf{b}(\bar{\omega}_{ik}) \otimes \mathbf{a}(\vartheta_x).
\tag{4.18}
$$

Equation (4.18) is consistent with the clutter space-time snapshot defined in $[5, 13]$ when the array is linear. The clutter covariance matrix

$$
\begin{aligned}
\mathbf{R}_c = \varepsilon\{\boldsymbol{\chi}_c \boldsymbol{\chi}_c^H\} &= \sigma^2 \sum_{i=0}^{N_r-1} \sum_{k=0}^{N_c-1} \xi_{ik} \mathbf{b}(\bar{\omega}_{ik}) \mathbf{b}^H(\bar{\omega}_{ik}) \otimes \mathbf{c}(\theta_i, \phi_k) \mathbf{c}(\theta_i, \phi_k)^H \\
&= \sigma^2 \sum_{i=0}^{N_r-1} \sum_{k=0}^{N_c-1} \xi_{ik} \mathbf{b}(\bar{\omega}_{ik}) \mathbf{b}^H(\bar{\omega}_{ik}) \otimes \mathbf{a}(\vartheta_x) \mathbf{a}^H(\vartheta_x)
\end{aligned}
\tag{4.19}
$$

is also consistent with the clutter covariance matrix defined in $[5, 13]$ as

$$
\mathbf{R}_c = \sigma^2 \sum_{i=0}^{N_r-1} \sum_{k=0}^{N_c-1} \xi_{ik} \mathbf{e}(\vartheta_z) \mathbf{e}^H(\vartheta_z) \otimes \mathbf{b}(\bar{\omega}_{ik}) \mathbf{b}^H(\bar{\omega}_{ik}) \otimes \mathbf{a}(\vartheta_x) \mathbf{a}^H(\vartheta_x)
\tag{4.20}
$$

when the array is linear.

4.2 Planar Array

The steering vectors, space-time snapshots, and covariance matrices are structured differently in the radar model presented in Chapter III than the model in [5]

Table 4.1:   This table contains the parameters used for the planar array simulations. The simulations are performed to verify the new model in Chapter III is consistent with the original model in [5].

Variable	Value	Variable	Value
M	32 pulses	R	66 km
N	36	N_c	NM
Azimuth Channels	6	β	1
Elevation Channels	6	γ	-3 dB
f_o	1240 MHz	Array Transmit Gain	22 dB
d_x	$\lambda/2$	Element Pattern	Cosine
d_z	$\lambda/2$	Element Gain	4 dB
f_r	1984 Hz	Element Backlobe Level	-30 dB
Time Delay	0.8 μs	Transmit Taper	Uniform
P_t	200 kW	System Losses L_s	3 dB
B	800 kHz	Target ϕ	0°
F_n (Noise Figure)	3 dB	Target θ	0°
h_a (aircraft altitude)	3073 m	Target $\bar{\omega}$	0.25
v_a (aircraft velocity)	120 m/s		

when the array is planar. Therefore, computer simulation is done to verify that both models produce identical results when the array is planar and has uniform element spacing. The array used for model verification is a 6 × 6 uniformly spaced array containing 36 elements. Performance metrics include output SINR versus normalized Doppler frequency plots and detection probability versus input SINR per element per pulse plots. All simulation parameters in this section are given in Table 4.1.

4.2.1 Antenna Array Pattern.   Prior to simulating the performance metrics, the array pattern is plotted to ensure it is consistent between both models. The array pattern is converted from radar coordinates to cartesian coordinates using each model and is plotted in Fig. 4.1. The array center is located at the origin ($x = 0$, $y = 0$, $z = 0$). As expected, most energy is focused straight out of the array at boresight with symmetric sidelobes and nulls. The interference models are examined next since they are directly affected by the array pattern.
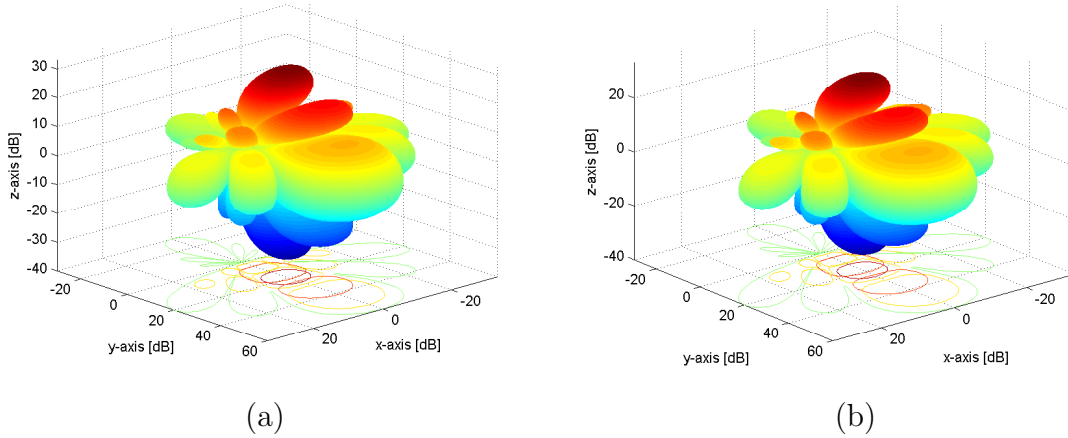
Figure 4.1:   Normalized array pattern in cartesian coordinates for a uniformly spaced 6×6 element array using the (a) new Chapter III model and (b) the original model in [5]. The array center is located at the cartesian coordinate system origin in this plot.

4.2.2 Covariance Matrices.   Once the array pattern is verified, the co-variance matrices are checked for consistency. The rank of each covariance matrix is examined by plotting the sorted eigenvalues of each matrix. The rank of a matrix equals the number of nonzero eigenvalues. Since the noise covariance matrix is identical in both models as discussed in Chapter III, it is not examined. The noise covariance matrix is simply a scaled identity matrix whose size is determined by the number of array elements and pulses. The jammer and clutter matrices, however, are structured differently for each model and must be compared. The clutter matrix rank according to `Matlab`® is 109 for both radar models and its sorted eigen-value plot is shown in Fig. 4.2. The Brennan clutter rank prediction is 148 for each clutter matrix. The Brennan rank prediction is defined for a planar array in [3] as rank$(\mathbf{R}_c) \approx \lfloor N + (M-1)\beta \rfloor \min(P, N_r + 1)$ where N is the number of azimuth channels, P is the number of elevation channels, N_r is the number of ambiguous range rings, and β was discussed in Chapter II. A dashed line is drawn at the Brennan rank prediction to show where the matrix eigenvalues should go to zero. The jammer matrix rank is 32 for both models and its sorted eigenvalue plot is shown in Fig. 4.3. Both models produce very similar sorted eigenvalue plots for each matrix, verifying
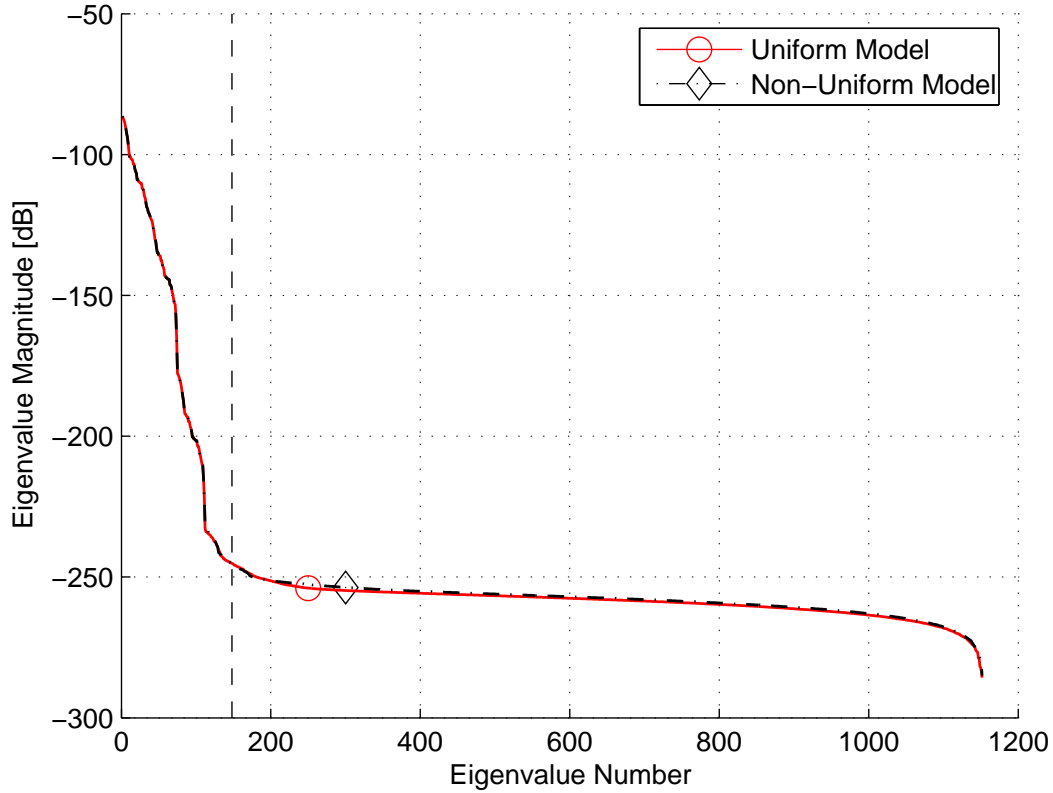
47

Figure 4.2: Clutter matrix sorted eigenvalue magnitudes for a 6×6 array with $\beta = 1$. The clutter matrix from each model is plotted on the same plot to illustrate they are nearly identical. The Brennan rank prediction shown by the dashed line is 148 while Matlab® gives the matrix rank as 109 in both cases.

that the covariance matrices in each model are the same. Although the eigenvalue magnitudes of each model in Fig. 4.3 are not identical, the important part of the this plot is that the eigenvalue magnitudes drop at the same point.

4.2.3 STAP Algorithms. The matched filter, adaptive matched filter, JDL, and FTS STAP methods must also be verified since they are used in simulations in the following chapter. Output SINR and detection probability plots are used to compare each STAP method for both models. All figures shown overlay the simulation results from each model. The matched filter response is verified first as shown in Fig. 4.4. The matched filter output SINR is plotted as an ideal performance metric. Each STAP
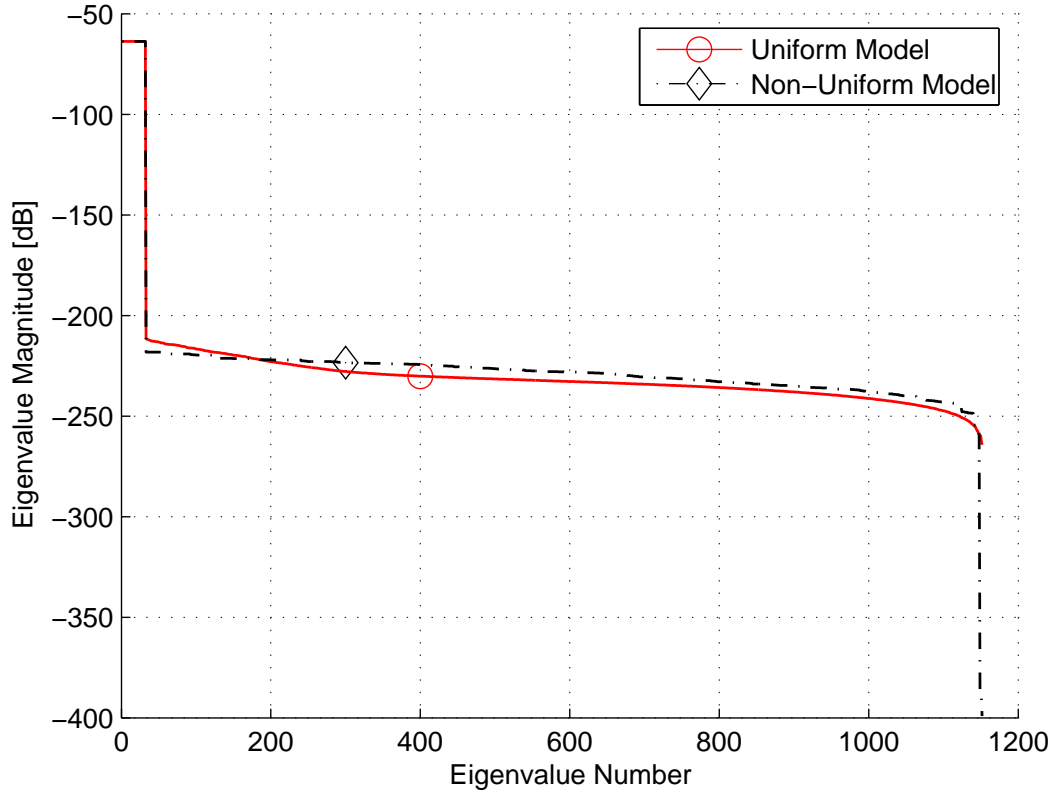
Figure 4.3: Jammer matrix eigenvalue magnitudes for a 6×6 array. Each matrix produces a very similar sorted eigenvalue magnitude plot. The matrix rank is given as 32 by `Matlab`® in each case.

method attempts to achieve the same performance, with reduced sample support, as the matched filter. The two models produce the same results for the matched filter output SINR. Output SINR peaks at about 31 dB. Figure 4.5 shows the output SINR versus normalized Doppler frequency plot using the JDL method. The JDL algorithm results are plotted using $12 \times 4 \times 6 = 288$ and $4 \times 3 \times 6 = 72$ degrees of freedom in Doppler, azimuth, and elevation, respectively. As expected, SINR degrades as the number of degrees of freedom decreases. Figure 4.6 is another plot verifying the JDL algorithms from each radar model produce the same results. Detection probability is plotted versus input SINR per element per pulse for the adaptive matched filter and the JDL method using 1000 realizations of χ under estimated covariance. The false alarm probability P_{fa} is 0.01. The false alarm probability means a target will be
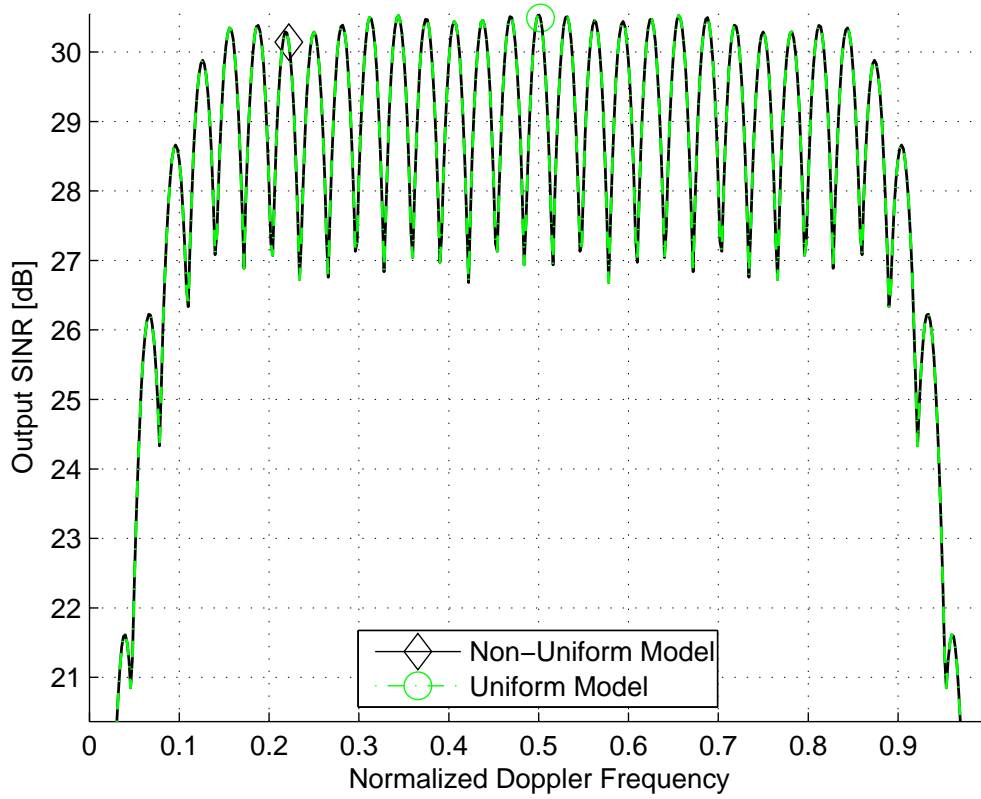
Figure 4.4:   Output SINR plot using the matched filter under known clutter covariance for a 6×6 array.

detected one out of every 100 times when there really is no target present. Again, the adaptive matched filter is an ideal performance metric to evaluate JDL performance. JDL performs slightly worse than the adaptive matched filter, as expected. The JDL algorithm requires about 2 dB more input SINR than the adaptive matched filter to obtain the same detection probability. The simulation of each model was performed separately, producing unique realizations of χ. Therefore, covariance matrix estimates for each model are not based on identical realizations of χ, resulting in the small variations seen in detection probability. However, the detection probability results are close enough for model verification.

The other STAP method to be verified is FTS. Again, output SINR and detection probability plots are used to check that the FTS algorithm modified in Chap-
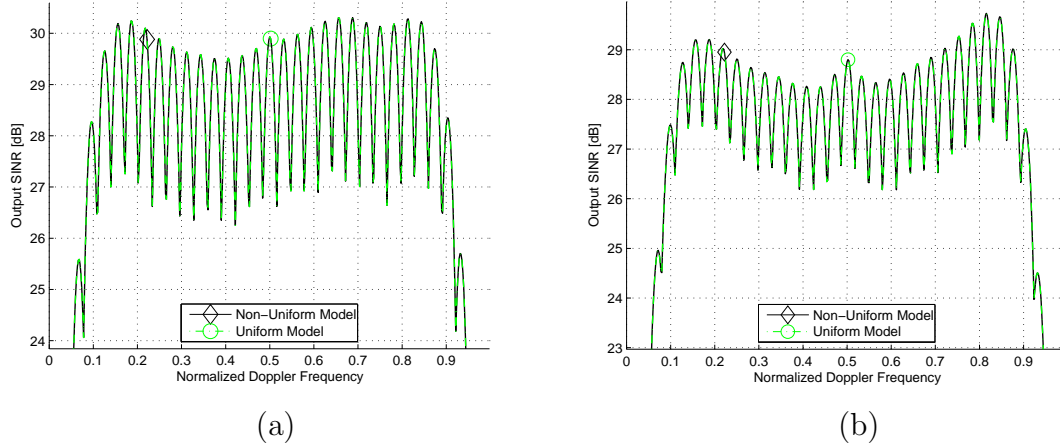
Figure 4.5:   Output SINR plot of the JDL method under known clutter covariance for a 6×6 array. The JDL algorithm in (a) uses $12 \times 4 \times 6 = 288$ degrees of freedom and (b) uses $4 \times 3 \times 6 = 72$ degrees of freedom in Doppler, azimuth, and elevation. Output SINR degrades as the number of degrees of freedom decreases.

ter III is consistent with the FTS algorithm in [5]. The simulated FTS algorithm uses a Blackman-Harris window across Doppler. Figure 4.7 shows the output SINR versus normalized Doppler frequency plot for the FTS method. FTS performance is notably worse than the matched filter, as expected, since FTS is not adaptive across Doppler. Figure 4.8 shows the detection probability versus input SINR plot verifying the FTS and adaptive matched filter. As expected, FTS does not perform as well as the adaptive matched filter. FTS requires about 7 dB more input SINR than the adaptive matched filter to obtain the same detection probability.

4.3   Summary

The new radar model presented in Chapter III is consistent with the model in [6, 13] for the uniformly spaced linear array and the model in [5] for the uniformly spaced planar array. This model can now used with confidence to simulate non-uniformly spaced arrays. The next chapter uses the model to simulate circular arrays and arrays with failed elements.
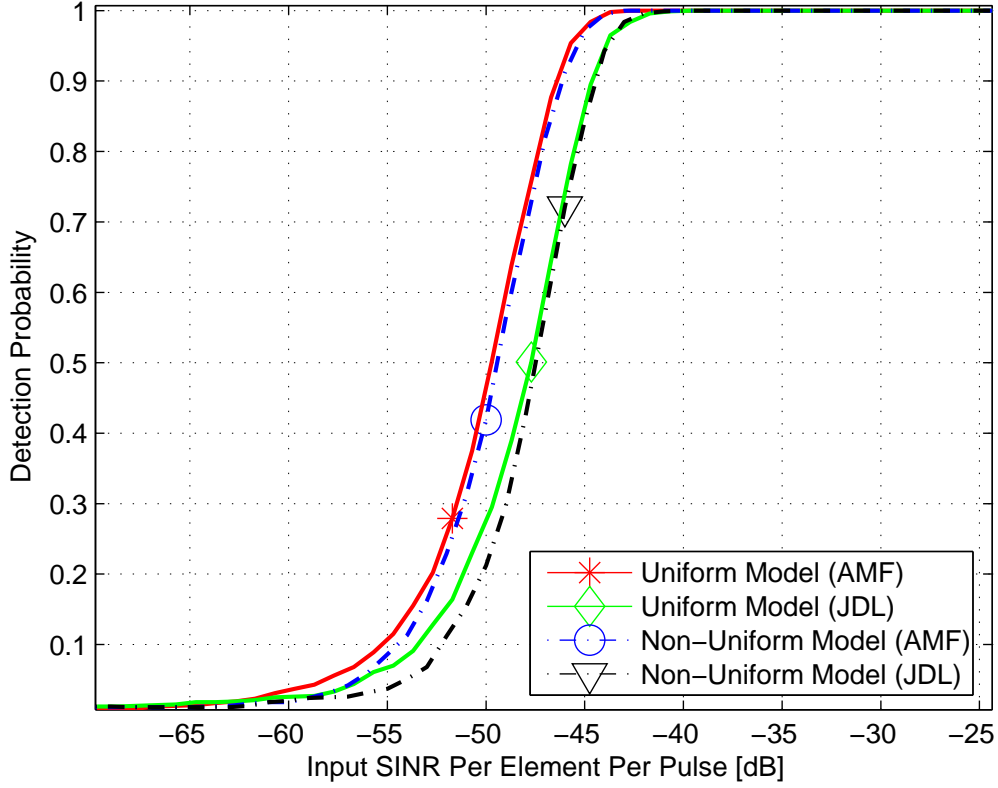
Figure 4.6: Detection probability for the JDL method and adaptive matched filter under estimated clutter covariance for a 6×6 array using 1000 realizations of $\boldsymbol{\chi}$, $P_{fa} = 0.01$, and $\bar{\omega} = 0.25$. The JDL algorithm here uses $4 \times 3 \times 6 = 72$ degrees of freedom in Doppler, azimuth, and elevation. The JDL algorithm performs very well, only slightly worse than the adaptive matched filter.
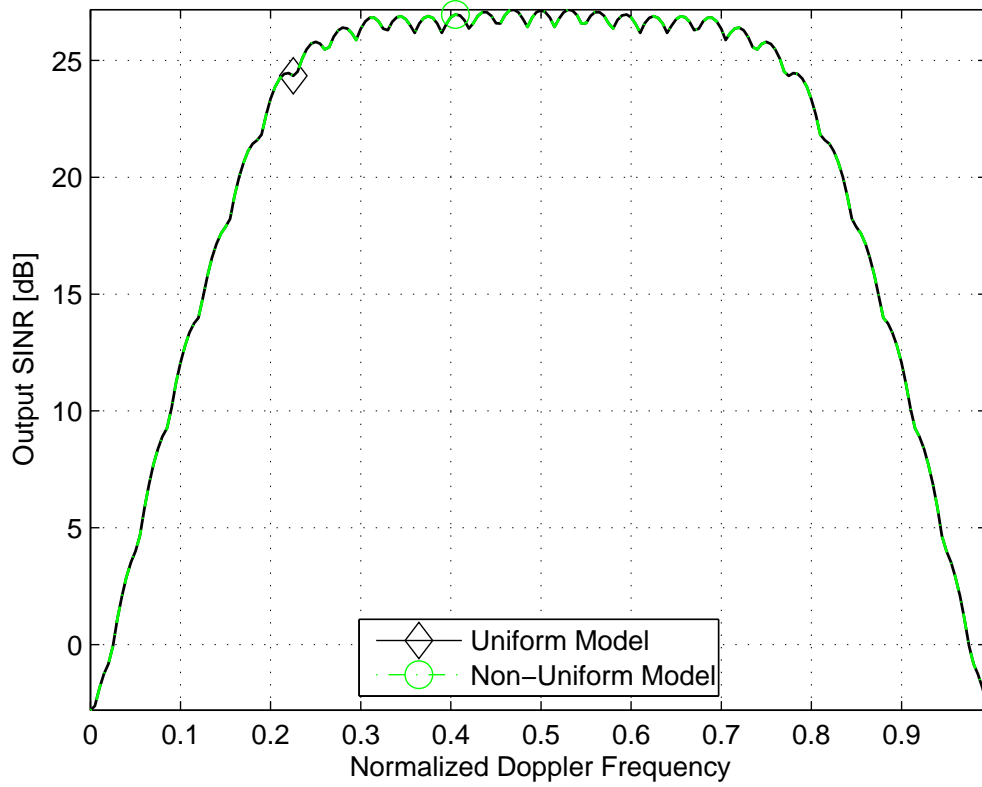
Figure 4.7: Output SINR plot of the FTS method under known clutter covariance for a 6×6 array. A Blackman-Harris window is applied across Doppler in the FTS algorithm here to compensate for its inability to adapt across Doppler.
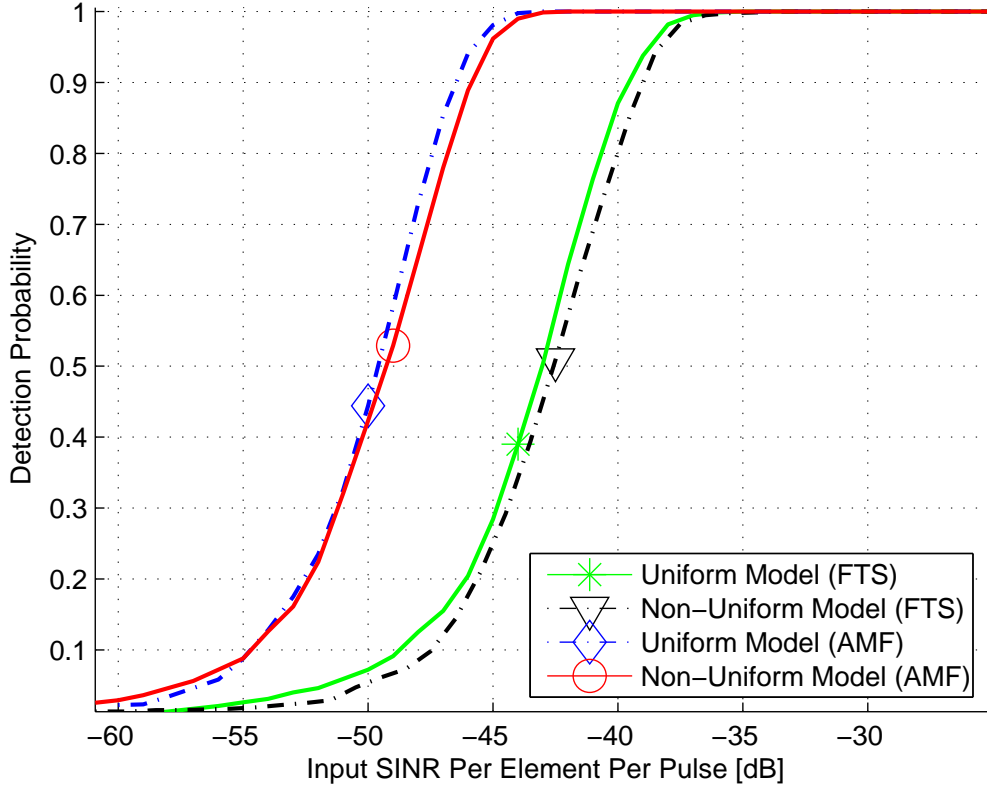
Figure 4.8: Detection probability for adaptive matched filter and FTS method with a Blackman-Harris window across Doppler under estimated clutter covariance for a 6×6 array using 1000 realizations of $\boldsymbol{\chi}$, $P_{fa} = 0.01$, and $\bar{\omega} = 0.25$. FTS needs about 7 dB more input SINR per element per pulse to obtain the same detection probability as the adaptive matched filter.

V. Non-Uniform Array Performance Evaluation

This chapter uses the model presented in Chapter III to examine the performance of certain non-uniformly spaced arrays using STAP techniques. There are infinitely many array configurations, so the circular array is one array configuration explored since it has been researched in the literature. The performance of each array is evaluated based on SINR loss plots and detection probability plots for the FTS algorithm, JDL algorithm, and matched filter. SINR loss is plotted instead of output SINR since the simulated arrays have different numbers of elements. Output SINR increases when more elements are in the array. SINR loss is a measure of actual output SINR to maximum output SNR. Maximum output SNR refers to the thermal noise only case. Therefore, SINR loss characterizes array efficiency regardless of the number of elements in the array. The antenna pattern of each array is also plotted to see the radiated energy and examine any sidelobes present. Power spectral density (PSD) plots are provided to illustrate the impact of non-uniformly spaced arrays on signal detection in the interference environment. Finally, the susceptibility of each array to element failure is examined. Output SINR is plotted versus normalized Doppler frequency to study array failure effects. Certain non-uniformly spaced array configurations may potentially incur less degradation than uniformly spaced planar arrays when elements fail. A 10% and 20% element failure rate is applied to each array and compared to array performance without element failure. Each non-uniformly spaced array is compared to a 6×6 uniform planar array with half wavelength inter-element spacing. The 6×6 array and non-uniformly spaced arrays have equal physical dimensions, 60.484 centimeters wide and 60.484 centimeters high. Comparisons are done to see if the circular arrays perform as well as the uniform 6×6 planar array having the same width and height. Non-uniform element spacing may allow the use of fewer elements in the array without sacrificing signal detection performance. All simulation parameters in this chapter are the same as the parameters given in Table 4.1 in Chapter IV unless otherwise specified.

5.1 Circular Array - 24 Elements

5.1.1 Configuration. The first non-uniformly spaced array being examined is a circular array containing 24 elements. The array is 60.484 centimeters wide and 60.484 centimeters high. The distance between each element is about 7.87 centimeters. Ideally, the elements should be spaced by $\lambda/2 = 12.10$ centimeters to prevent grating lobes. The element configuration of the 24 element circular array is shown in Fig. 5.1. The platform velocity vector is along the positive x-axis since the array is side-looking. The array extends into the negative x-axis and negative z-axis. The reference element in this circular array is located at the coordinate ($x = 0$ m, $z = -0.3024$ m). The reference element is located furthest to the left, or closest to the aircraft nose. The 24 elements are arranged such that there are 13 elevation
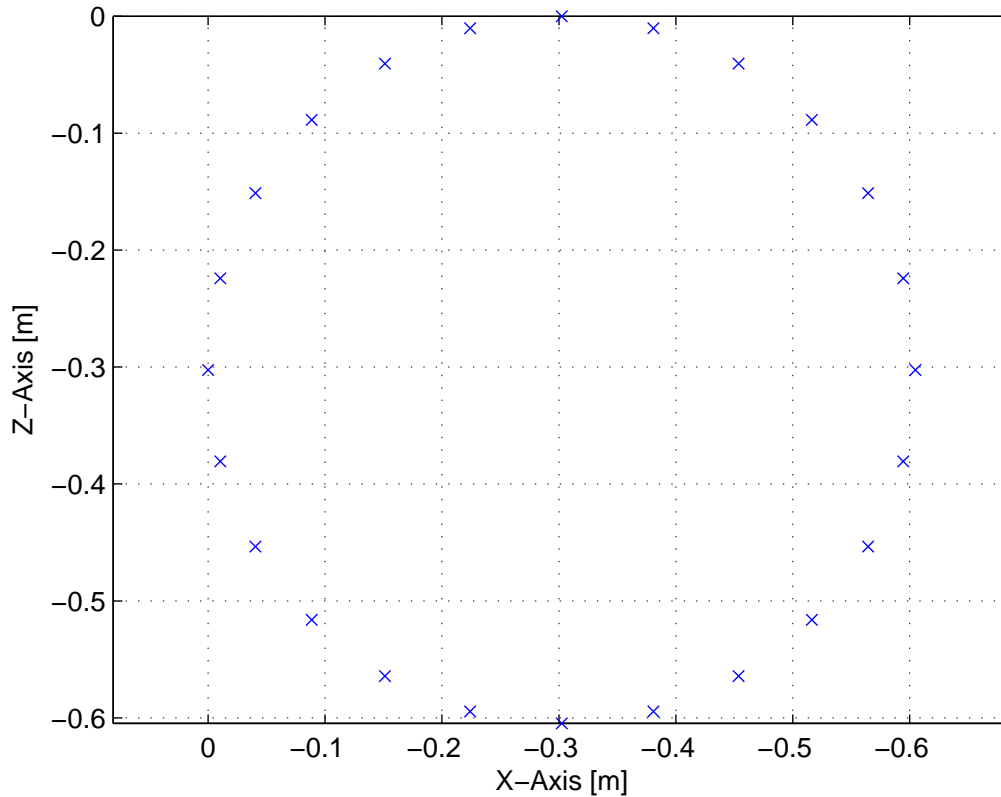

Figure 5.1:   Element positions of a side-looking circular array containing 24 elements. The platform velocity vector is along the positive x-axis, hence it is a sidelooking array.

56

channels and 13 azimuth channels. The 6×6 array has 6 elevation channels and 6 azimuth channels. The circular array has better angular resolution than the 6×6 array since the number of azimuth/elevation channels determines how well a target can be resolved in azimuth/elevation. For example, an array with only a few elevation channels might resolve a target within $\pm 15°$ of its actual elevation angle while an antenna with more elevation channels might be able to resolve a target within $\pm 5°$ of its actual elevation angle.

5.1.2 Array Pattern. The array pattern for the circular array is shown in Fig. 5.2. The array pattern is normalized and presented in cartesian coordinates since
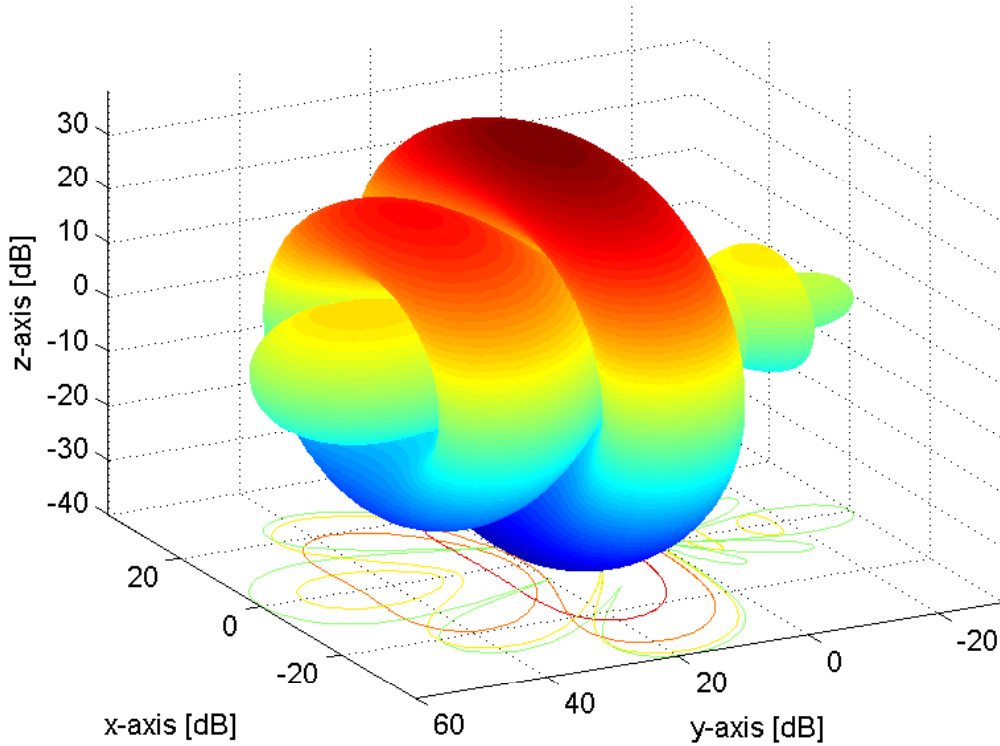

Figure 5.2: Normalized 3D array pattern converted from radar coordinates to cartesian coordinates for the 24 element circular array. The array center is located at the origin ($x = 0$, $y = 0$, $z = 0$). The element backlobe scaling factor is $b_e = -30$ dB.

cartesian coordinates give a more intuitive view of the pattern than radar coordinates. The sidelobes and nulls are circular in shape and wrap around the mainbeam. The sidelobes are about 9 dB below the mainbeam. The large sidelobes are undesirable because they illuminate clutter and other unwanted interference, making target detection more difficult. The small number of nulls is another disadvantage for the circular array because only a few azimuth and elevation angles can be nulled out to reduce interference, whereas the 6×6 uniform array in Fig. 4.1 has many more nulls.

5.1.3 Clutter Covariance Matrix. The clutter matrix sorted eigenvalue magnitudes for the circular array and uniform planar array are plotted to compare the impact of each array configuration on clutter rank. The matrix rank depends on
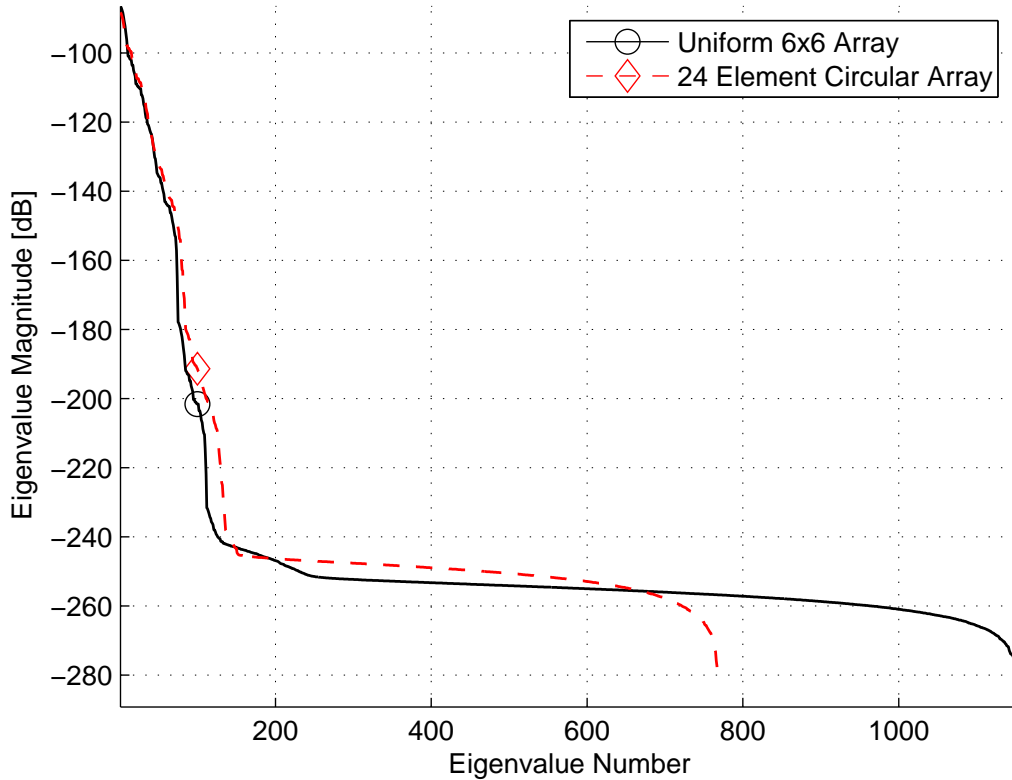

Figure 5.3: Clutter matrix sorted eigenvalue magnitudes for the 24 element circular array and the 6×6 planar array with $\beta = 1$. The clutter rank is similar for both arrays, meaning that the amount of interference due to clutter is only slightly different for each array.

the number of nonzero eigenvalues. Figure 5.3 shows the clutter rank comparison between the circular array and the uniform planar array. Clutter rank is not significantly higher for the circular array when compared to the uniform planar array in this case. Therefore, the amount of interference due to clutter is almost the same for both arrays. Clutter is just as difficult to suppress with the circular array as the uniform planar array since their clutter ranks are so similar. The slight difference in clutter rank between the two arrays can be attributed to a few different factors. First, more sidelobes from the circular array pattern illuminate more clutter than the uniform planar array. The circular array also has fewer nulls than the 6×6 array, so more interference is nulled out by the uniform planar array. Another factor contributing to the circular array's larger clutter rank is the element spacing. The 6×6 array has uniform inter-element spacing every half wavelength. Therefore, clutter samples are duplicated since each element moves a half wavelength per PRI. The circular array does not have uniform spacing, so new clutter samples are introduced each PRI.

   5.1.4   Power Spectra.   Figure 5.4 shows the signal match power spectra of the 24 element circular array and the uniform planar array. The signal match plot shows the signal received without any adaptivity. In other words, the signal match
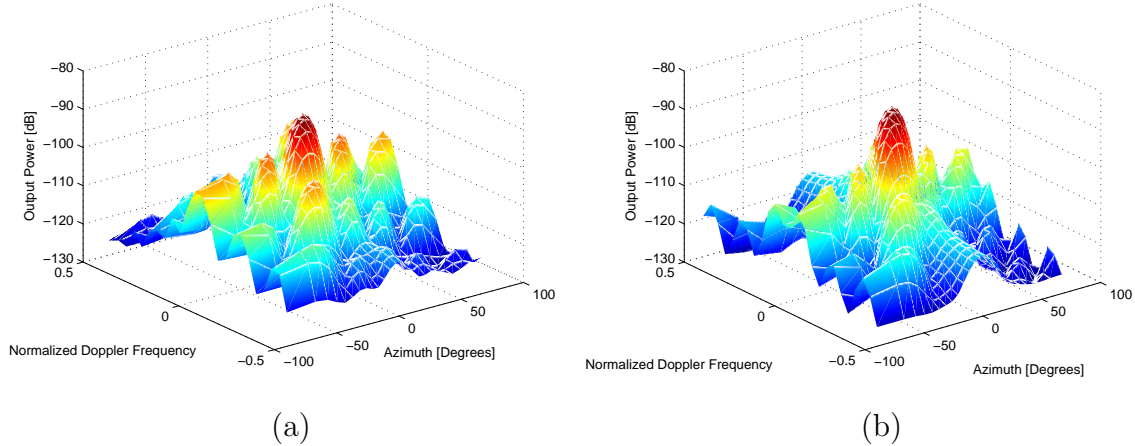

(a)   (b)

Figure 5.4:   Signal match power spectra for the (a) 24 element circular array using 32 pulses and the (b) 6×6 planar array using 32 pulses. There is more interference introduced by the large sidelobes from the circular array.
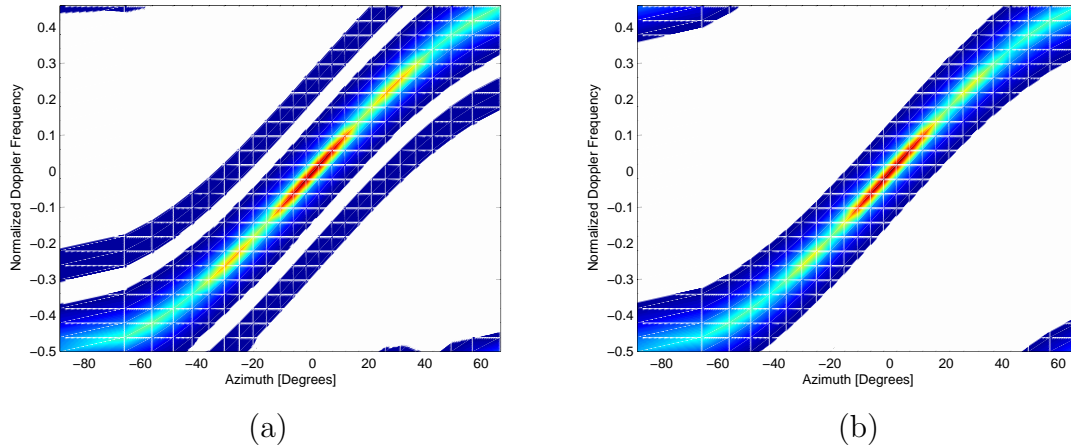
59

Figure 5.5: Minimum variance estimator power spectra for the (a) 24 element circular array using 32 pulses and the (b) 6×6 planar array using 32 pulses.

power spectra illustrates the signal return from the environment based purely on the array pattern. The signal match power spectra shows how interference such as clutter and noise is illuminated by the mainbeam and sidelobes. Comparing the two power spectra shows that more interference is introduced into the system when the array is circular. More interference results from the larger sidelobes in the circular array pattern and the non-uniform element spacing.

The MVE power spectra is shown in Fig. 5.5 for each array. The MVE power spectra simply illustrates the clutter location. The output power is not shown in the MVE power spectra because amplitude information is meaningless for this algorithm. Amplitude information is meaningless because MVE sacrifices amplitude estimation for high resolution interference location. As expected, most interference is located boresight to the array at 0 Doppler frequency. All other interference is along the clutter ridge.

5.1.5 Matched Filter. SINR loss versus normalized Doppler frequency plots are generated for the circular array. The 6×6 planar array SINR loss is also plotted along with the circular array SINR loss to compare the performance of each array. SINR loss shows the degradation of SINR due to correlated interference. The ideal
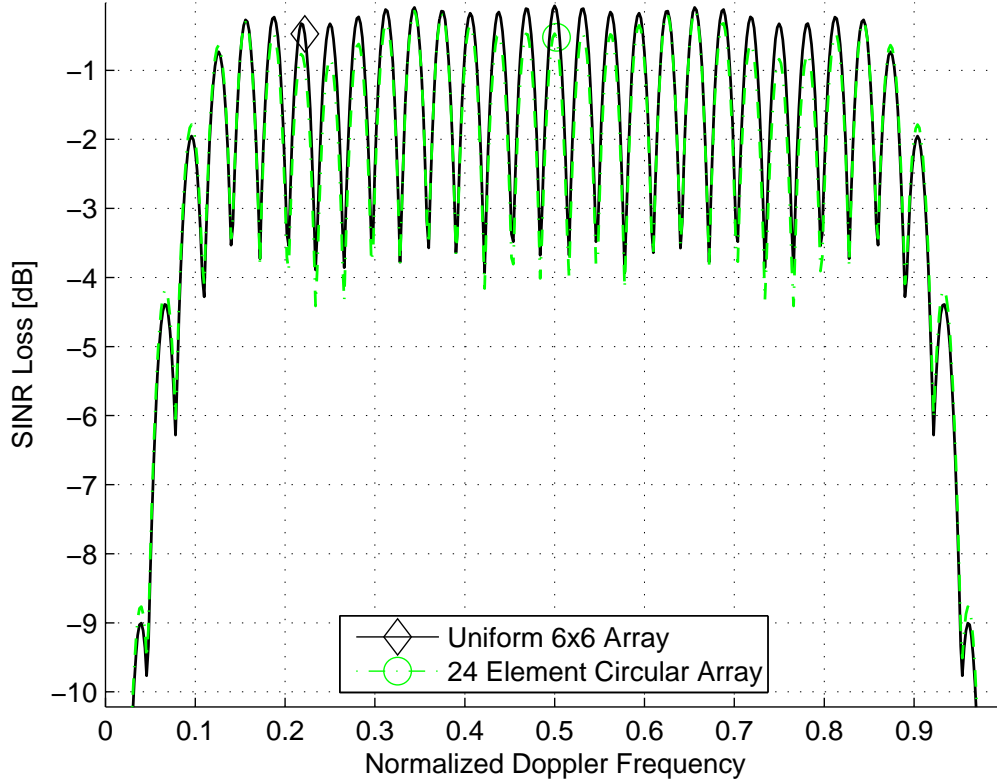
Figure 5.6: SINR loss using the matched filter for the 24 element circular array and the 6×6 uniform planar array. The SINR loss is very similar between the two arrays.

SINR loss is 0 dB, however correlated sources such as clutter and jammers degrade SINR. Therefore, the thermal noise only case is a theoretical performance bound used to measure the amount of degradation caused by correlated interference sources.

The first SINR loss plot is the matched filter scenario shown in Fig. 5.6. The matched filter is fully adaptive and represents the best performance possible for each array. The output SINR for the uniform planar array is about 2 dB higher than the output SINR for the circular array across all Doppler frequencies since it has 12 more elements. SINR tapers off at the same Doppler frequency for each array, meaning the minimum and maximum discernable velocities are the same for each array. Figure 5.6 shows the 24 element circular array and the 6×6 uniform array have very similar SINR losses due to interference when using the matched filter STAP algorithm. The

24 element circular array is efficient when compared to the uniform 6×6 array because it has 12 fewer elements, yet practically suppresses correlated interference as well as the uniform planar array.

5.1.6   JDL Algorithm.   The SINR loss plot in Fig. 5.7 compares the circular array and uniform planar array using the JDL algorithm. The JDL algorithm used in this simulation has $4 \times 3 \times 6 = 72$ degrees of freedom in Doppler, azimuth, and elevation, respectively. The reduced degrees of freedom degrade output SINR, causing higher SINR losses, when compared to the matched filter output SINR. The 6×6
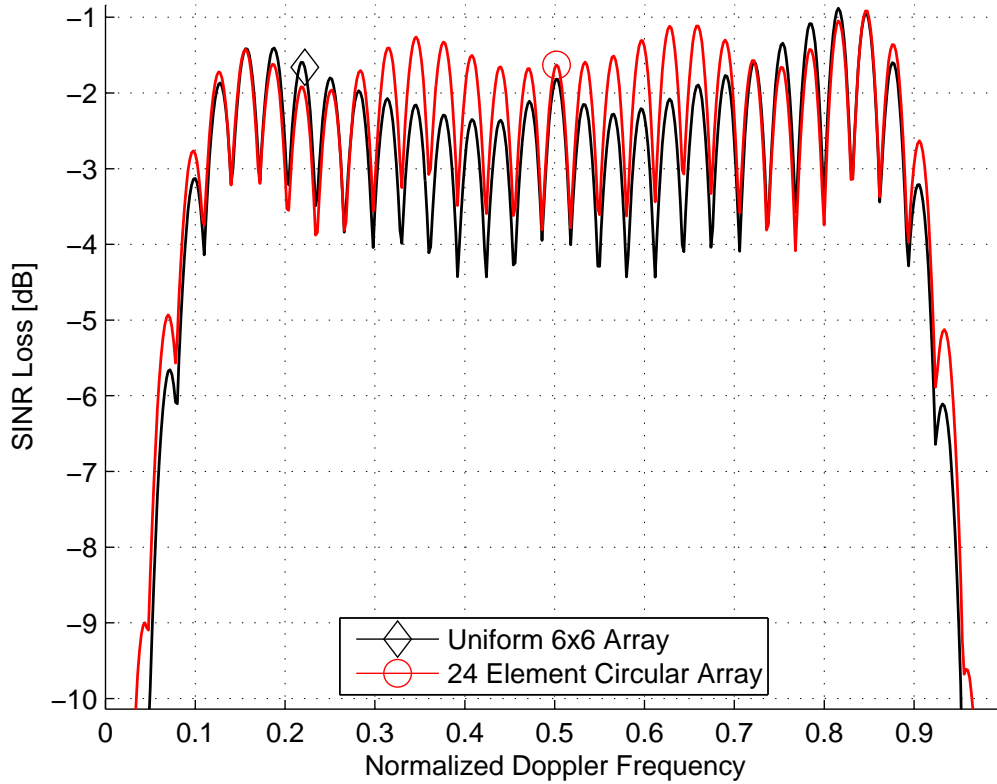

Figure 5.7:   SINR loss using the JDL algorithm for the 24 element circular array and the 6×6 planar array. The JDL algorithm implemented here uses $4 \times 3 \times 6 = 72$ degrees of freedom in Doppler, azimuth, and elevation, respectively. The 6×6 uniform array has about 1 dB more SINR loss than the circular array along the clutter null and between 0.3 and 0.7 normalized Doppler frequency.

uniform array has slightly more SINR loss than the 24 element circular array along the clutter null and between the normalized Doppler frequencies 0.3 and 0.7. However, the difference in SINR loss is only about 1 dB in those regions mentioned. The circular array suppresses correlated interference slightly better than the uniform planar array when using the JDL STAP method. Therefore, the circular array suppresses correlated interference more efficiently than the uniform planar array using the partially adaptive JDL STAP algorithm.

Detection probability is plotted versus input SINR per element per pulse in Fig. 5.8 for both arrays using the JDL algorithm and the adaptive matched filter.
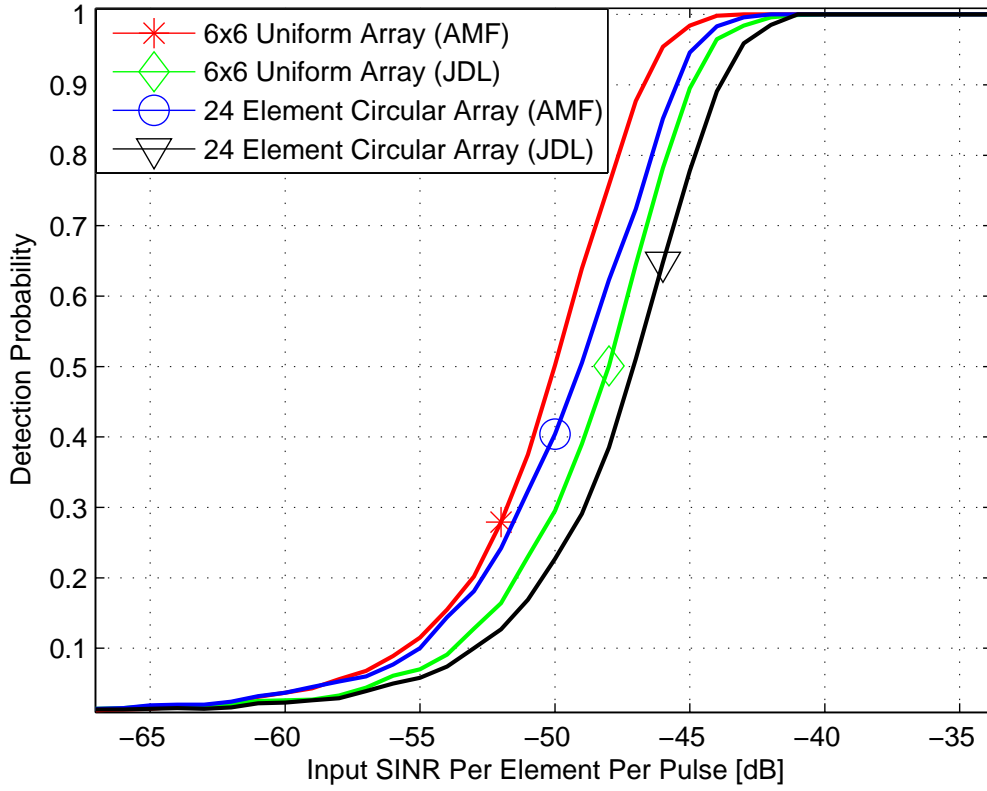

Figure 5.8: Detection probability plot using the JDL algorithm for the 24 element circular array and the 6×6 planar array under estimated clutter covariance using 1000 realizations of $\boldsymbol{\chi}$, $P_{fa} = 0.01$, and $\bar{\omega} = 0.5$. The JDL algorithm in this case uses $4 \times 3 \times 6 = 72$ degrees of freedom in Doppler, azimuth, and elevation, respectively.

Again, the JDL algorithm here uses $4 \times 3 \times 6 = 72$ degrees of freedom in Doppler, azimuth, and elevation, respectively. A normalized Doppler frequency of 0.5 is used in this plot. The circular array has slightly less SINR loss than the uniform 6×6 array at $\bar{\omega} = 0.5$. The plot shows the 24 element circular array requires approximately 1 dB more input SINR per element per pulse to achieve the same detection probability as the 6×6 array for both STAP methods. Fewer elements in the circular array provide less integration gain than the uniform 6×6 array, resulting in the small difference in detection probability. The adaptive matched filter requires about 2 dB less input SINR per element per pulse than the JDL algorithm to obtain the same detection probability for both arrays. The JDL algorithm provides good detection probability for both arrays since it performs so closely to the adaptive matched filter.

5.1.7 FTS Algorithm. Figure 5.9 shows the SINR loss plot for each array using the FTS algorithm. A Blackman-Harris window is applied across Doppler. The window attempts to improve performance since FTS cannot adapt across Doppler. The narrow range of discernible velocities is a result of the FTS algorithm's inability to adapt across Doppler. SINR loss for the 24 element circular array is about 1 dB more than the uniform 6×6 array SINR loss when using the FTS algorithm. The FTS method SINR loss is about 3 dB more than the JDL method SINR loss across its discernible velocity range. The JDL method has a wider range of discernible velocities than the FTS method for both arrays.

Detection probability is plotted in Fig. 5.10 using the FTS algorithm and AMF for both arrays. The 24 element circular array requires about 3 dB more input SINR per element per pulse to obtain the same detection probability as the uniform 6×6 array when using the FTS algorithm. The FTS algorithm requires about 8 dB more input SINR per element per pulse to obtain the same detection probability as the AMF for the circular array. The 6×6 uniform array requires about 6 dB more input SINR per element per pulse when using the FTS algorithm to obtain the same detection probability as the AMF. These results indicate the 24 element circular array
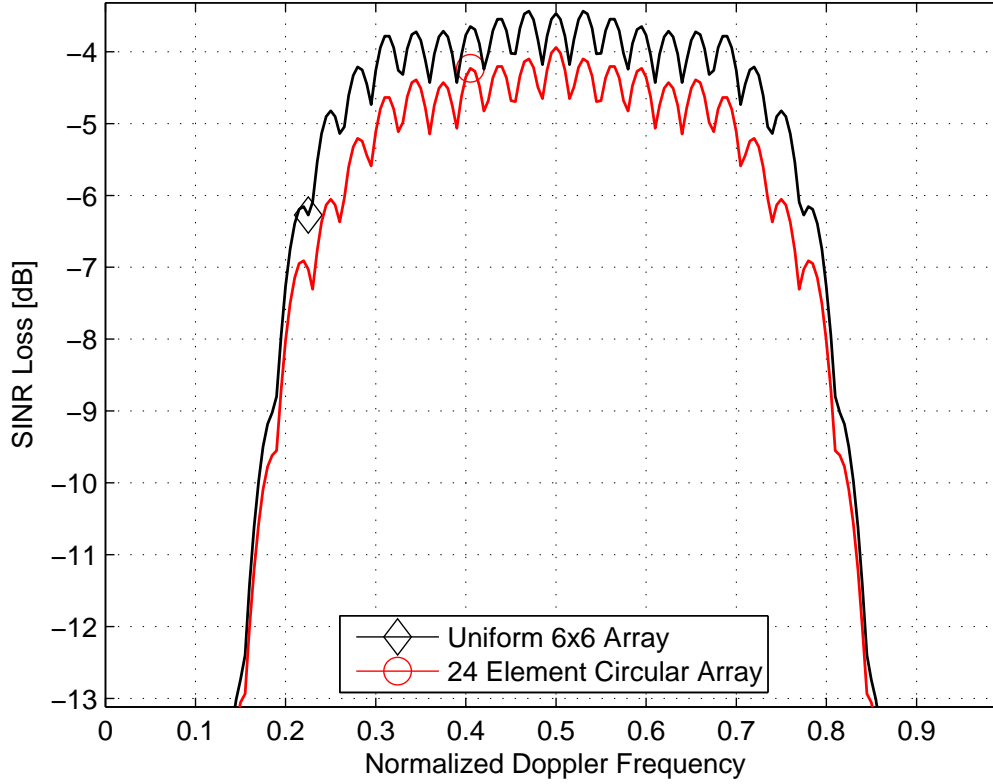
Figure 5.9: SINR loss using the FTS algorithm for the 24 element circular array and the 6 × 6 planar array. A Blackman-Harris window is applied across Doppler since FTS cannot adapt across Doppler. The circular array has about 1 more dB of SINR loss than the 6 × 6 uniform array across the discernible Doppler frequency range.

suffers slightly more than the uniform planar array when using the partially adaptive FTS STAP method. Input SINR per element per pulse must be increased by roughly 7 dB using the FTS algorithm to obtain the same detection probability as the JDL algorithm for the circular array. The uniform 6 × 6 array requires about 5 dB more input SINR per element per pulse when using the FTS algorithm to obtain the same detection probability when using the JDL algorithm. The reason FTS requires a higher input SINR than the other two algorithms is because FTS is not adaptable across Doppler. The FTS method cannot suppress as much interference as the JDL
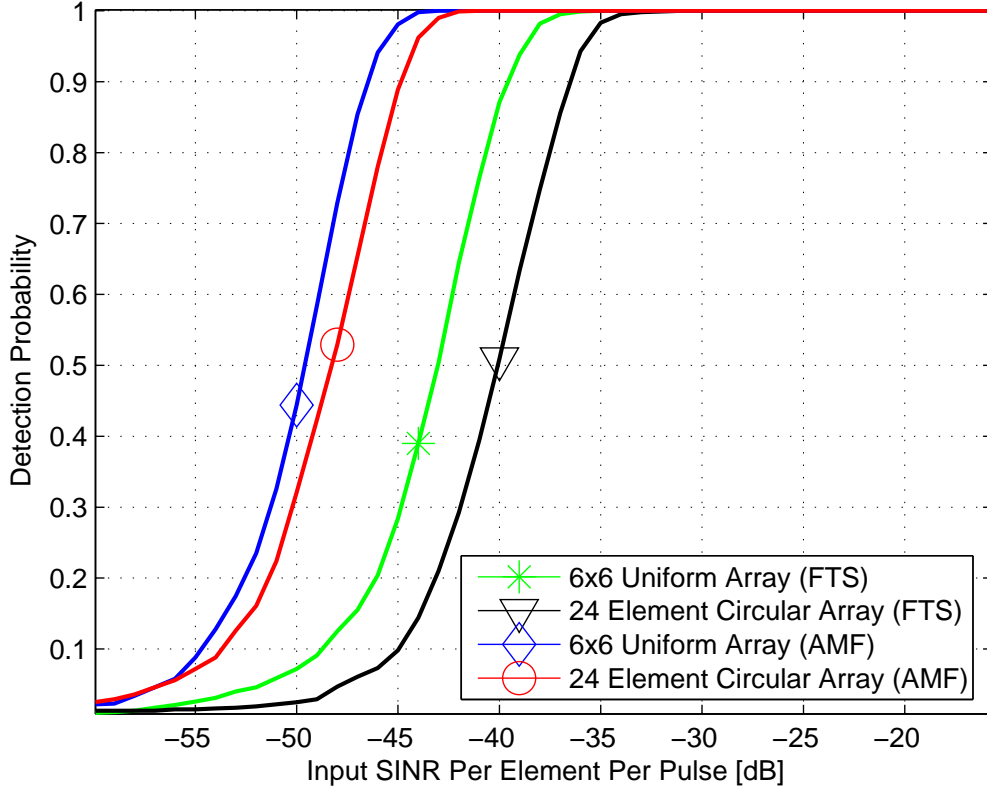
Figure 5.10:   Detection probability plot using the FTS algorithm and AMF for the 24 element circular array and the 6×6 planar array under estimated clutter covariance using 1000 realizations of $\boldsymbol{\chi}$, $P_{fa} = 0.01$, and $\bar{\omega} = 0.5$. The FTS algorithm here employs a Blackman-Harris window across Doppler.

method. Therefore, signal strength must be increased if the FTS algorithm is to be used.

5.1.8   Summary.   The 24 element circular array performance is similar to the 6×6 uniform array. The circular array clutter rank is slightly higher than the uniform planar array clutter rank due to the larger sidelobes and non-uniform spacing. SINR loss is very similar for both arrays when using the matched filter. SINR loss is actually higher for the uniform 6×6 array than the 24 element circular array when using the JDL algorithm. This result indicates the circular array mitigates correlated interference more efficiently than the uniform 6×6 array under the simulation parameters.

The 24 element circular array requires about 1 dB more input SINR per element per pulse than the uniform planar array to obtain the same detection probability as the uniform planar array when using the JDL method. The circular array provides correlated interference mitigation and detection probability comparable to the uniformly spaced 6×6 array using the JDL and AMF STAP techniques. The circular array suffers higher losses than the uniform 6×6 array when using the FTS technique. The performance metrics clearly demonstrate the 24 element circular array is an efficient array when compared to the uniform 6×6 array.

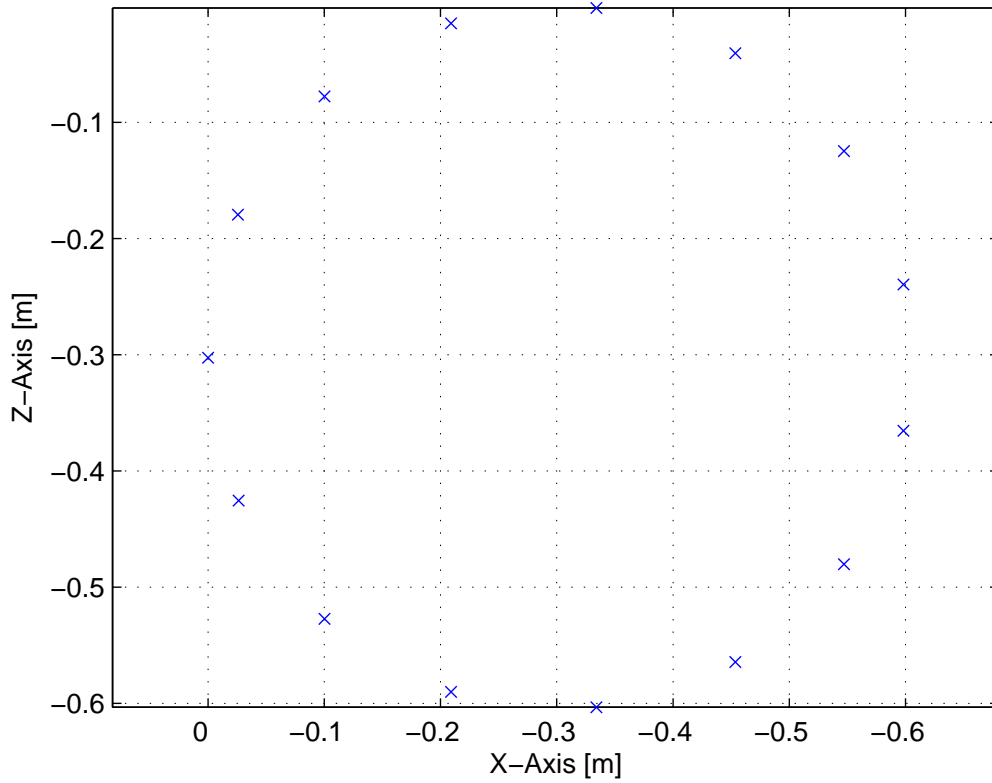## 5.2 Circular Array - 15 Elements

Figure 5.11: Element positions of a side-looking circular array containing 15 elements. The platform velocity vector is along the positive x-axis. The spacing between each element is about half a centimeter longer than half a wavelength.

5.2.1 Configuration. The next array compared to the 6×6 uniform planar array is a 15 element circular array shown in Fig. 5.11. Both arrays have the same width and height again. The 15 element circular array is chosen because the distance between each element is very close to half a wavelength. In fact, the distance between each element is almost half of a centimeter longer than half a wavelength. The inter-element spacing is chosen to prevent grating lobes. The element positions are arranged such that there are 9 different channels in azimuth and 15 different channels in elevation. The 15 element circular array pattern is not shown because it is practically identical to the 24 element circular array pattern. The sidelobes are circular and are about 9 dB below the mainbeam. The clutter rank plot is also approximately the same for the two different circular arrays. The 15 element circular array clutter rank is only slightly higher than the uniform planar array clutter rank. Larger sidelobes and non-uniformly spaced elements increase clutter rank by introducing more interference from clutter.

5.2.2 Power Spectra. The signal match and MVE power spectra for the 15 element circular array and the uniform planar array are compared in Figs. 5.12 and
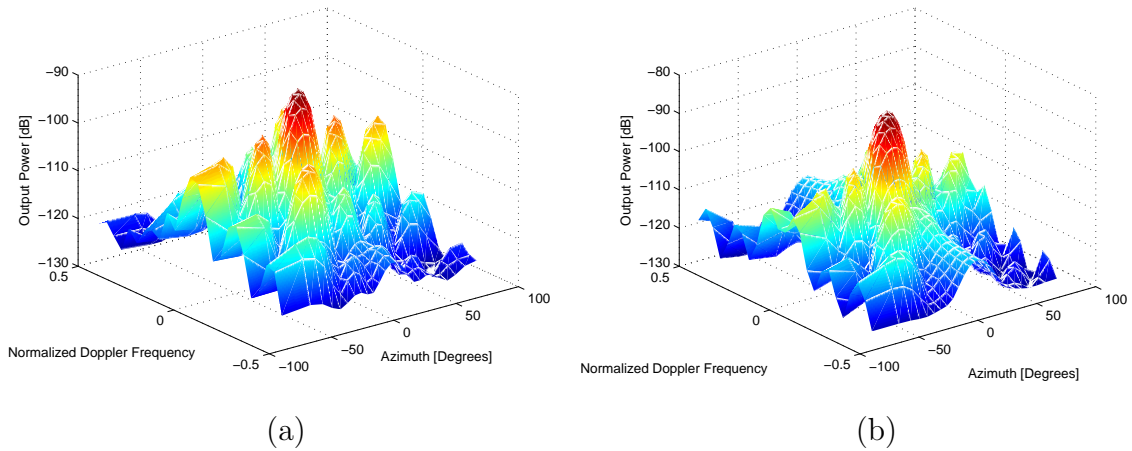

(a)   (b)

Figure 5.12: Signal match power spectra for the (a) 15 element circular array using 32 pulses and the (b) 6×6 planar array using 32 pulses. The larger sidelobes on the circular array illuminate more interference in the environment than the uniform planar array.
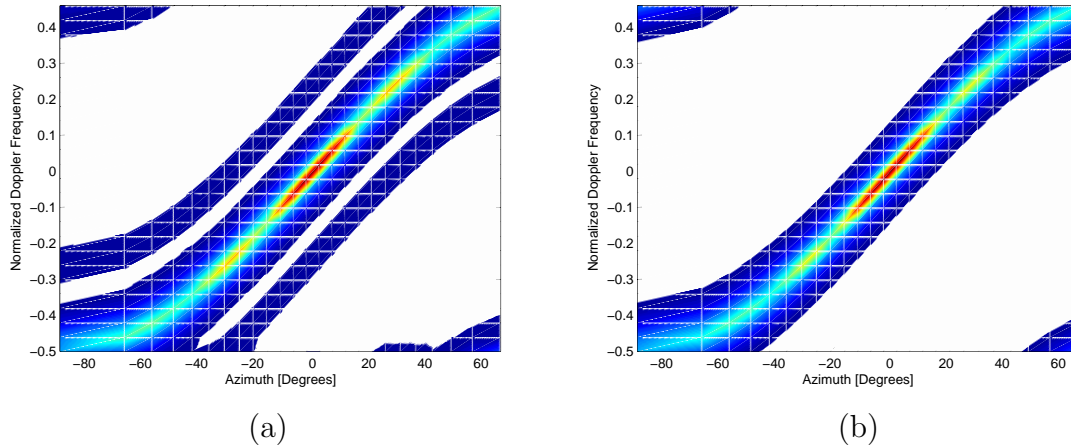
68

Figure 5.13:   Minimum variance estimator power spectra for the (a) 15 element circular array using 32 pulses and the (b) 6 × 6 planar array using 32 pulses.

5.13. The circular array introduces more interference than the uniform planar array because of its larger sidelobes and non-uniform element spacing. The signal match output power spectra for the 15 element circular array is below that of the 24 element circular array. This result makes sense since output SINR increases as the number of elements in the array increases. The 15 element circular array MVE power spectra is nearly identical to the 24 element circular array MVE power spectra. The majority of interference is located at 0 normalized Doppler frequency and 0° azimuth. All other interference is along the clutter ridge.

5.2.3   Matched Filter.   The matched filter SINR loss is plotted in Fig. 5.14 using the 15 element circular array and the uniform planar array. The circular array output SINR is about 4 dB below the uniform planar array output SINR due to the different number of elements. However, SINR loss from correlated interference is approximately the same for the two arrays across all Doppler frequencies. The 15 element circular array suppresses correlated interference very efficiently when compared to the uniform planar array using the matched filter since both arrays have approximately the same SINR losses yet the circular array has 21 fewer elements. SINR loss ranges from 0 to 4 dB across the discernible velocity range due to Doppler filter straddling losses.
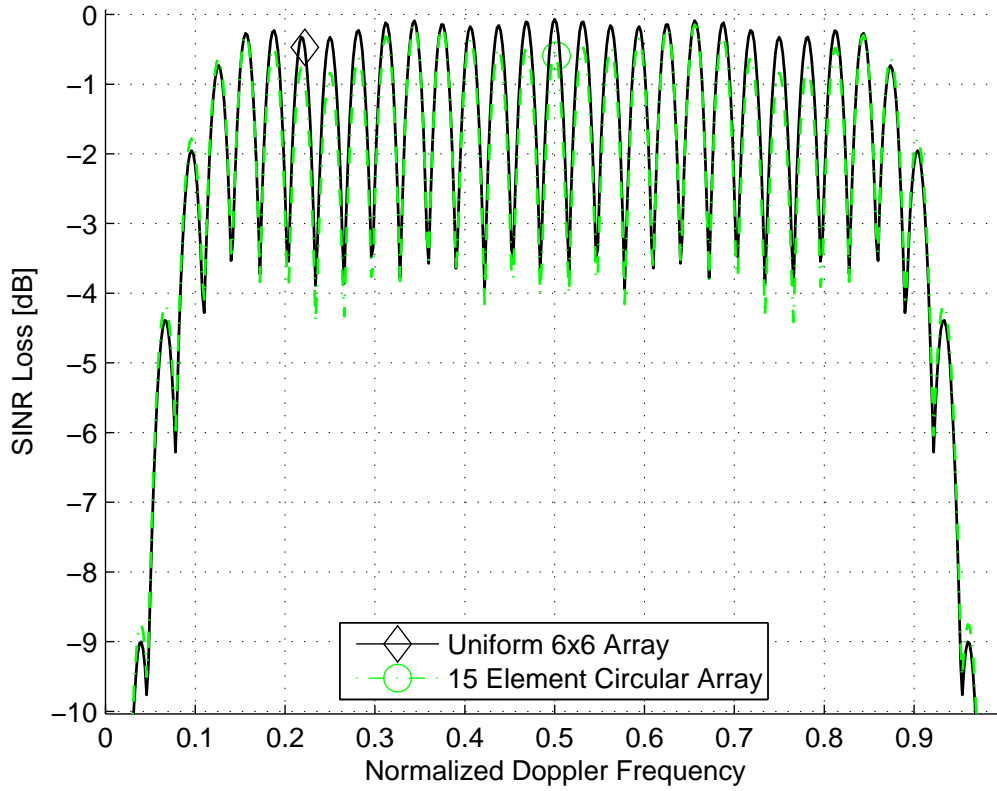
69

Figure 5.14: SINR loss using the matched filter for the 15 element circular array and the 6×6 uniform planar array. SINR losses are very similar for both arrays.

5.2.4 JDL Algorithm. The JDL algorithm is used for the SINR loss plot in Fig. 5.15. There are $4 \times 3 \times 6 = 72$ degrees of freedom in Doppler, azimuth, and elevation, respectively. The circular array suppresses correlated interference quite well when compared to the uniform planar array using the JDL algorithm. The uniform planar array loses about 1 dB more SINR than the 15 element circular array around the clutter null and between normalized Doppler frequencies 0.3 and 0.7. The 15 element circular array suppresses correlated interference better than the uniform planar using the partially adaptive JDL technique. Also, the JDL algorithm results in roughly 1 dB more SINR loss than the matched filter for both arrays.

Detection probability is plotted in Fig. 5.16 for the 15 element circular array and uniform planar array using the JDL and AMF algorithms. There are $4 \times 3 \times 6 =$
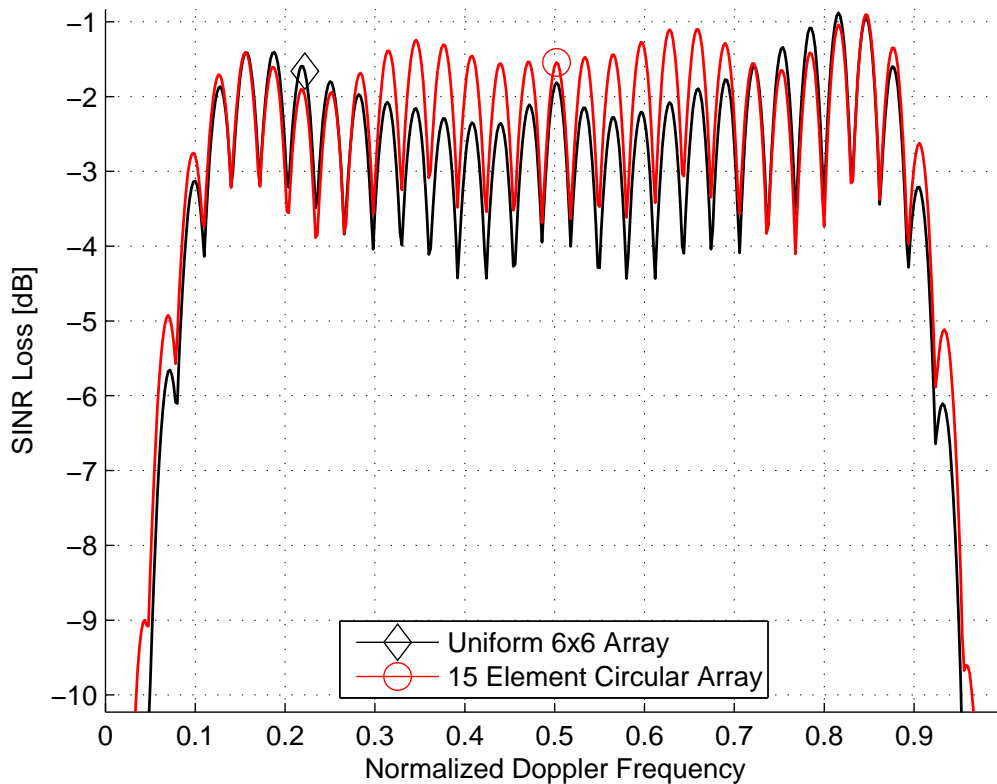
Figure 5.15: SINR loss using the JDL algorithm for the 15 element circular array and the 6×6 planar array. The JDL algorithm implemented here uses $4 \times 3 \times 6 = 72$ degrees of freedom in Doppler, azimuth, and elevation, respectively. The uniform planar array has about 1 dB more SINR loss than the circular array between 0.3 and 0.7 normalized Doppler frequency.

72 degrees of freedom in Doppler, azimuth, and elevation, respectively. Detection probability is evaluated at a normalized Doppler frequency of 0.5. At 0.5 normalized Doppler frequency, the uniform 6×6 array has slightly more SINR loss than the circular array. The circular array requires about 4 dB more input SINR per element per pulse to obtain the same detection probability as the uniform 6×6 array when using the AMF. The circular array requires about 3 dB more input SINR per element per pulse to obtain the same detection probability as the uniform planar array using the JDL algorithm. These results indicate the circular array performs well when using the JDL STAP algorithm.
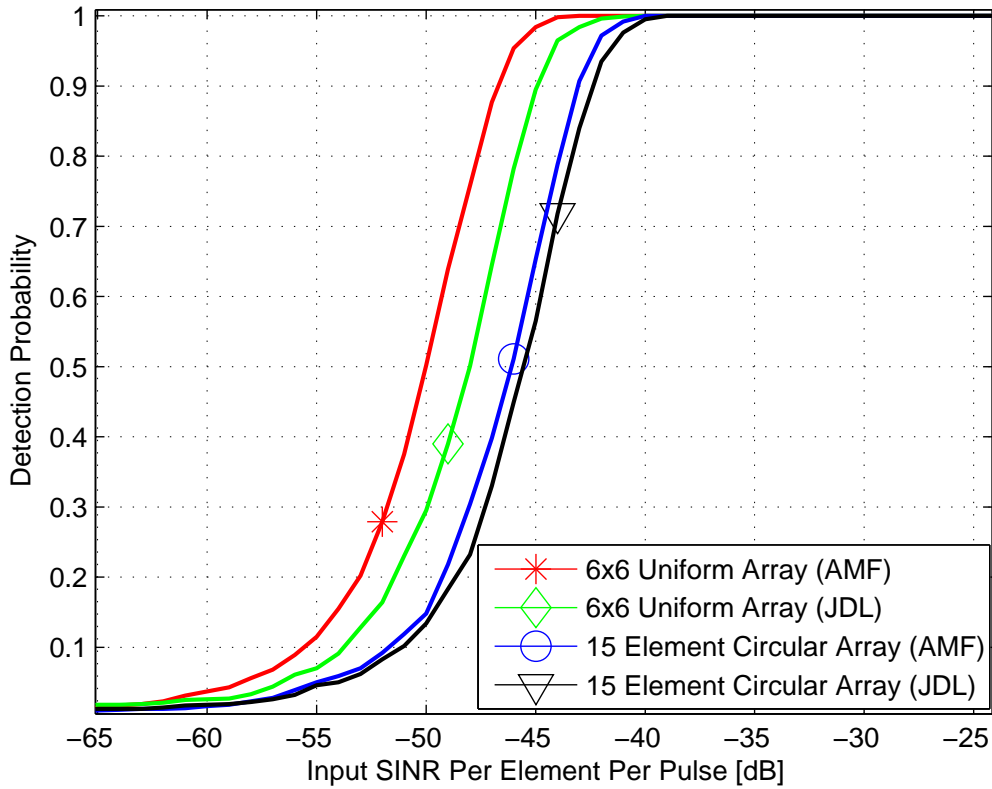
Figure 5.16: Detection probability plot using the JDL algorithm for the 15 element circular array and the 6×6 planar array under estimated clutter covariance using 1000 realizations of $\boldsymbol{\chi}$, $P_{fa} = 0.01$, and $\bar{\omega} = 0.5$. The JDL algorithm in this case uses $4 \times 3 \times 6 = 72$ degrees of freedom in Doppler, azimuth, and elevation, respectively.

5.2.5 FTS Algorithm. The FTS algorithm is used for the SINR loss plot in Fig. 5.17 for the 15 element circular array and the uniform planar array. A Blackman-Harris window is applied across Doppler again. SINR loss for the 15 element circular array is about the same as SINR loss for the 24 element circular array when using the FTS method. SINR loss for the 15 element circular array is about 1 dB lower than the uniform 6×6 array. There is about 4 to 6 dB SINR lost across the discernible velocity range for the circular array due to correlated interference. As expected, the discernible velocity range is quite narrow when using the FTS algorithm because FTS
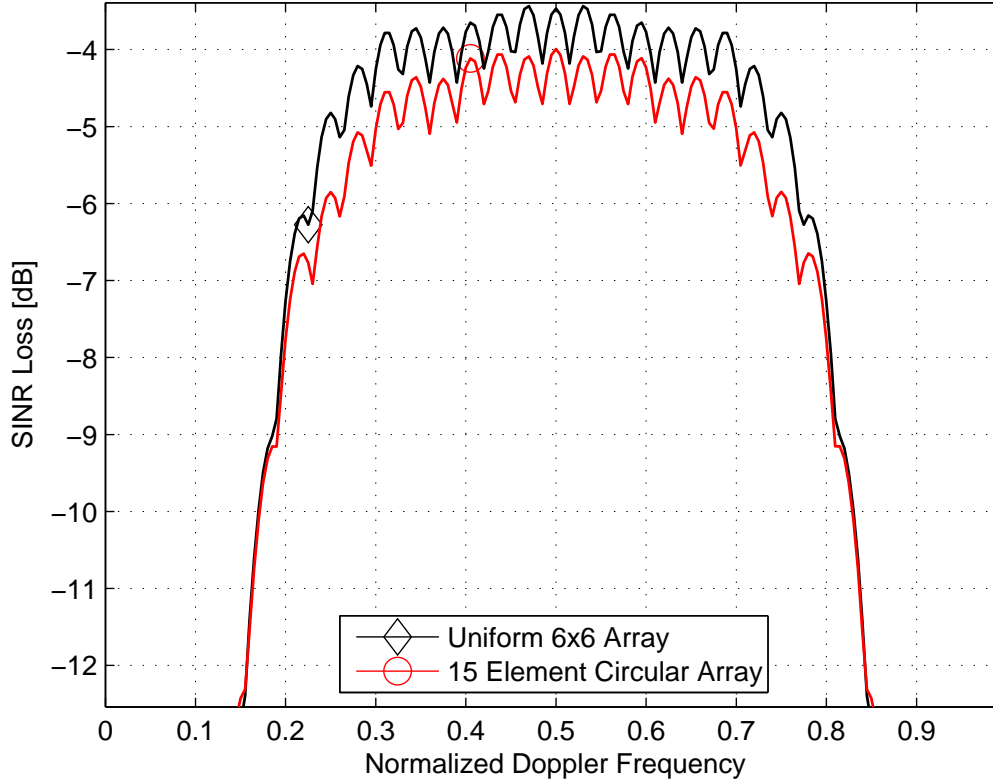
Figure 5.17:   SINR loss using the FTS algorithm for the 15 element circular array and the 6×6 planar array. A Blackman-Harris window is applied across Doppler since FTS cannot adapt across Doppler.

is not adaptable in Doppler. The discernible velocity range is roughly 0.2 to 0.8 normalized Doppler frequency.

Detection probability is plotted in Fig. 5.18 using the FTS and adaptive matched filer algorithms for both arrays. The FTS algorithm performs notably worse than the adaptive matched filter for both arrays. The FTS method requires about 7 dB more input SINR per element per pulse to obtain the same detection probability as the AMF for the uniform 6×6 array. For the 15 element circular array, the FTS method requires about 9 dB more input SINR per element per pulse to obtain the same detection probability as the AMF. The circular array suffers more than the uniform 6×6 array when using the FTS algorithm.
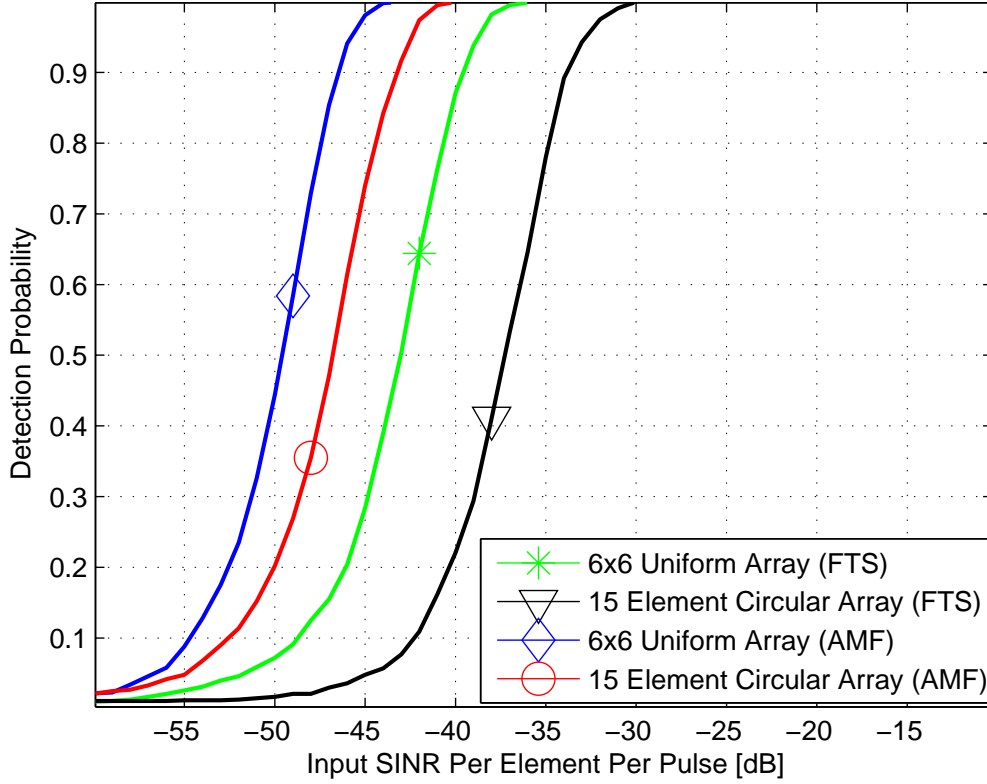
Figure 5.18: Detection probability plot using the FTS algorithm for the 15 element circular array and the 6×6 planar array under estimated clutter covariance using 1000 realizations of $\boldsymbol{\chi}$, $P_{fa} = 0.01$, and $\bar{\omega} = 0.5$. The FTS algorithm here employs a Blackman-Harris window across Doppler.

5.2.6 Summary. The 15 element circular array performance is very similar to the 24 element circular array performance. The clutter rank for the 15 element circular array is slightly higher than the uniform 6×6 array clutter rank. Both arrays have the practically the same SINR loss when using the matched filter. When using the JDL algorithm, SINR loss for the uniform 6×6 array is roughly 1 dB higher than the 15 element circular array SINR loss between 0.3 and 0.7 normalized Doppler frequency. The 15 element circular array requires about 3 dB more input SINR per element per pulse to obtain the same detection probability as the uniform 6×6 array using the JDL algorithm. Under the FTS method, the 15 element circular array

74

does not perform as well as the uniform planar array. The 15 element circular array mitigates correlated interference as well as the uniform 6×6 array using the matched filter and JDL STAP techniques. The 15 element circular array also provides good detection probability considering the small number of elements. Therefore, results indicate the 15 element circular array performs efficiently when compared to the uniform 6×6 array.

5.3 Array Failure

Array failure is briefly explored here since array performance may vary according to array configuration. Output SINR averaged over 500 realizations is plotted versus normalized Doppler frequency using the matched filter to characterize the performance of each array. The failed elements are randomly chosen for each realization. The purpose here is to determine the susceptibility of each array to element failure. In all simulations, the array gain is kept the same, meaning SNR is constant despite failing elements. In reality, SNR would decrease if some elements failed to transmit because signal power would decrease. However, a constant SNR isolates degradations caused by changes in the array pattern such as grating lobes, a wider mainbeam, larger sidelobes, and different sidelobe and null locations. Different clutter patches are illuminated as a result of element failure. Element failure rates of approximately 10% and 20% are used in all simulations. Actual failure rates depend on the number of elements in the array. A more robust array will not be significantly impacted when some of its elements fail to operate.

5.3.1 6×6 *Array.*   The first array examined is the 6×6 uniformly spaced array. Average output SINR is plotted in Fig. 5.19 when 0, 4, and 7 elements fail. Actual failure rates are 11% and 19% when 4 and 7 elements fail, respectively. Output SINR peaks at about 30.5 dB when no elements fail. Output SINR degrades by about 1 dB across the discernible velocity range for approximately 10% of element failure. Output SINR degrades at a quicker rate around the clutter null with element failure.
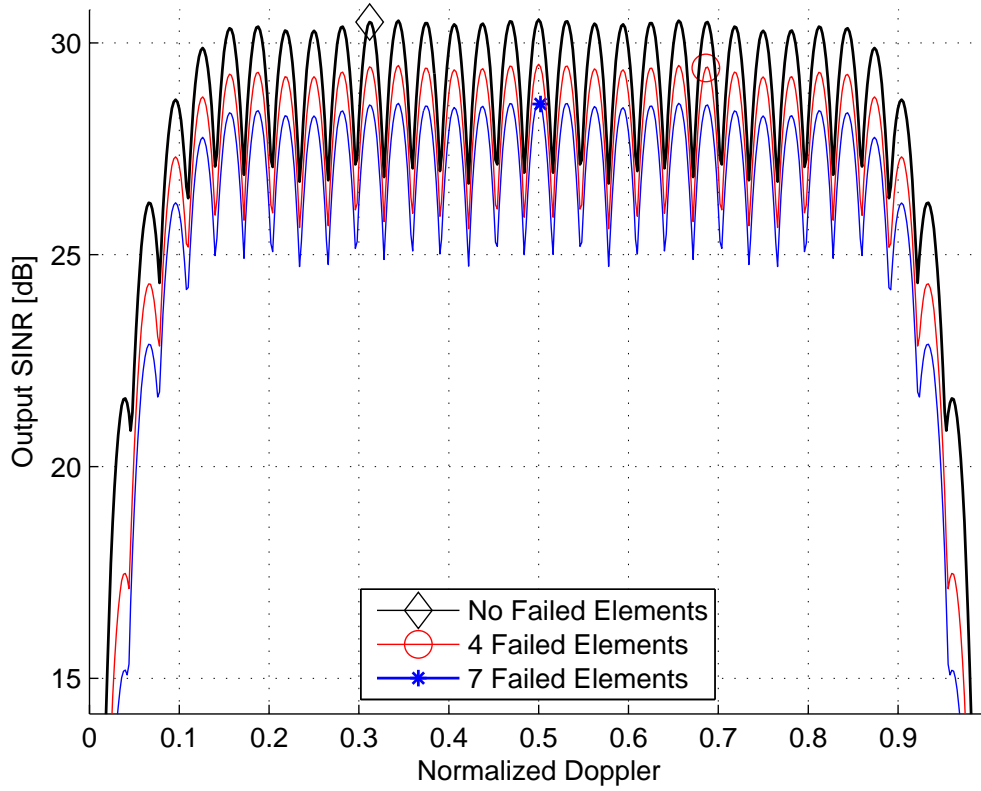
Figure 5.19: Average output SINR from the matched filter is plotted for the uniformly spaced 6×6 array with 0, 4, and 7 failed elements. Output SINR is averaged over 500 hundred realizations with the designated number of random elements failing during each realization and SNR = 1.

A Doppler frequency of 0.04 sees about a 4 dB degrade in output SINR from the 0% to 11% element failure rate and about 2.5 dB from the 11% to 19% failure rate.

5.3.2 24 Element Circular Array. The next array examined is the 24 element circular array. Figure 5.20 shows average output SINR plotted when 0, 3, and 5 elements fail. Actual failure rates are 13% and 21% when 3 and 5 elements fail, respectively. Output SINR peaks at about 28.5 dB with no elements failing. Output SINR degrades by about 1.3 dB across the discernible velocity range from the 0% to 13% element failure rate. From a 13% to 21% element failure rate, the 24 element circular array output SINR degrades about 1 dB. At the clutter null, output SINR
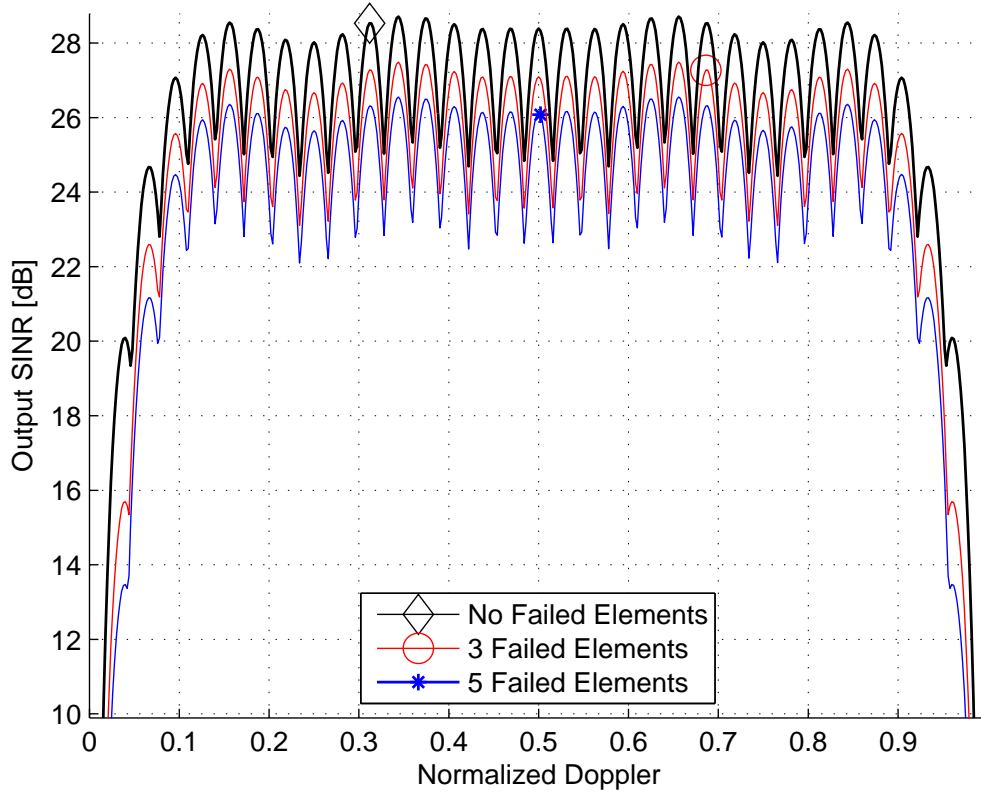
Figure 5.20:   Average output SINR from the matched filter is plotted for the 24 element circular array with 0, 3, and 5 failed elements, as labelled. Output SINR is averaged over 500 hundred realizations with the designated number of random elements failing during each realization and SNR = 1.

degrades at the same rate as the 6×6 array. The non-uniform circular configuration introduces fluctuations in peak output SINR across all Doppler frequencies with element failure.

5.3.3   15 Element Circular Array.   The last array examined is the 15 element circular array. Figure 5.21 shows average output SINR plotted when 0, 2, and 3 elements fail. Actual failure rates are 13% and 20% when 3 and 5 elements fail, respectively. Output SINR degradation is quite similar to the 24 element circular array. With a 0% element failure rate, output SINR peaks at about 26.5 dB for the 15 element circular array. Output SINR degrades by about 1.4 dB across the
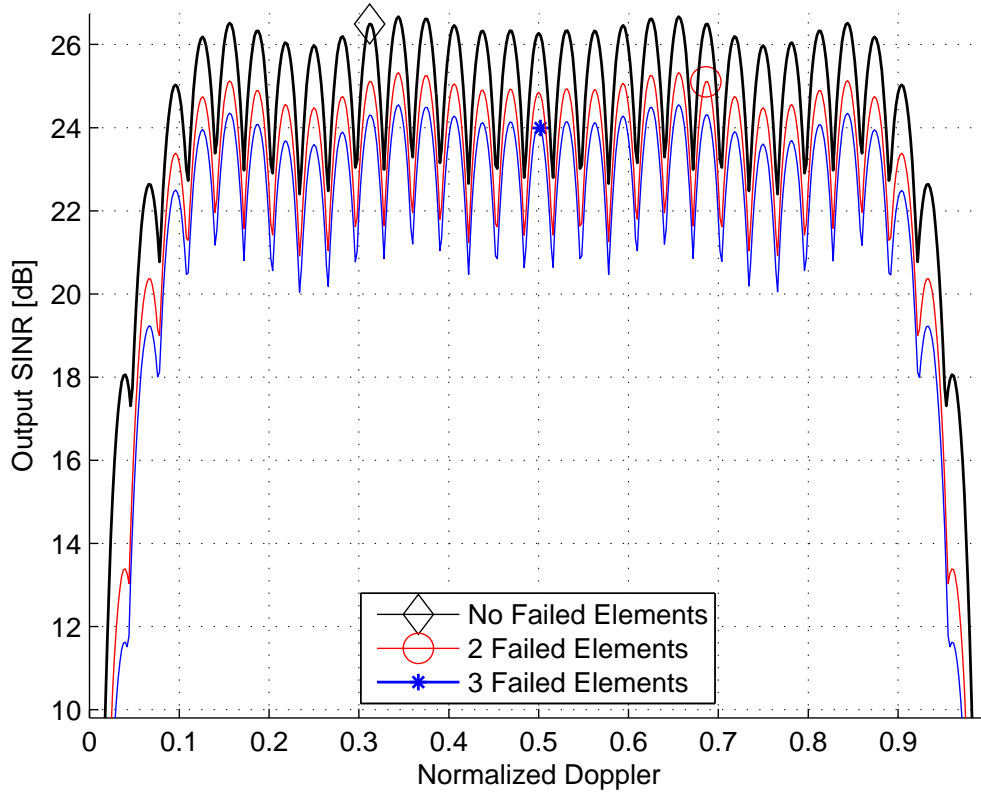
77

Figure 5.21:   Average output SINR from the matched filter is plotted for the 15 element circular array with 0, 2, and 3 failed elements, as labelled. Output SINR is averaged over 500 hundred realizations with the designated number of random elements failing during each realization and SNR = 1.

discernible velocity range from the 0% to 13% element failure rate. The 15 element circular array output SINR degrades by about 0.8 dB from the 13% to 20% element failure rate. At the clutter null, output SINR degrades at the same rate as the 6×6 array and 24 element circular array.

5.3.4 Summary.   The array failure plots demonstrate that output SINR performance degrades by approximately the same rate for the uniformly spaced 6×6 array and both circular array configurations. Output SINR degrades for all three arrays by roughly 1 dB from 0% to 10% and 10% to 20% element failure rates. All

three arrays also see higher losses in output SINR at the clutter null due to element failure.

5.4   Summary

The 15 element circular array and 24 element circular array have practically the same SINR losses for all three STAP algorithms used. Detection probabilities for each STAP method differ by roughly 2 dB input SINR per element per pulse for the two circular arrays. The SINR loss performance plots demonstrate that an array with fewer elements can suppress correlated interference as well as an array with more elements, depending on the configuration. JDL performs significantly better than FTS for the circular arrays and the uniform planar array. The JDL algorithm has a wider discernible velocity range, fewer SINR losses, and greater detection probability than the FTS algorithm for all arrays. Therefore, JDL is a valuable STAP method to use with circular arrays since it performs so well. The circular arrays mitigate correlated interference very efficiently using the matched filter and JDL algorithms since they have fewer elements than the uniform planar array, yet suffer roughly the same SINR losses. The circular arrays also suffer the same as the uniform 6×6 array in output SINR performance with element failure. Therefore, the circular array configuration is a considerable alternative to the uniformly spaced array when using STAP techniques for airborne radar systems.

VI. Conclusions

A n airborne radar model for non-uniformly spaced arrays has been developed and presented in Chapter III. The model is based on previous work in [5, 6, 13] and is valid for linear and planar arrays having arbitrary element locations. As it stands, a 3D array can be simulated using the model, however shadowing effects have not been included. Analysis of airborne radar systems with non-uniformly spaced arrays is valuable since non-uniformly spaced arrays may potentially provide better interference mitigation and target detection than uniformly spaced arrays. The model developed in this thesis provides the mathematical framework to evaluate any linear or planar array configuration using the matched filter, AMF, FTS, and JDL STAP techniques.

6.1   Airborne Radar Model For Non-Uniformly Spaced Arrays

The model development begins by introducing a new element position matrix $\mathbf{D}$ to accommodate arbitrary element locations in the array. This element position matrix creates a chain reaction affecting many components in the airborne radar model. First, the time/phase delay to each element changes since the elements can move to any location. Spatial frequencies change based on the time/phase delay, resulting in a new spatial steering vector $\mathbf{c}$. The array factor is restructured based on the new spatial steering vector. The space-time snapshot is reorganized since it contains the new spatial steering vector. Finally, the jammer and clutter covariance matrices are restructured due to the space-time snapshots. Two STAP techniques, JDL and FTS, are also updated so they can be applied to non-uniformly spaced arrays.

6.2   Model Verification

Verification of the airborne radar model for non-uniformly spaced arrays was accomplished in Chapter IV by inserting uniform element spacing into the model. The new model presented in Chapter III mathematically collapses back to the orig-

inal model of [6, 13] when the array is linear. Mathematical verification could not be accomplished for the uniform planar array due to the restructured steering vectors, space-time snapshots, and covariance matrices. Therefore, simulations were performed to compare the results produced from the new model in Chapter III and the original model in [5]. Simulations included array pattern plots, interference matrix eigenvalue magnitude plots, output SINR versus normalized Doppler frequency plots, and detection probability versus input SINR per element per pulse plots. Each model produced the same results, verifying their equivalence for the uniformly spaced planar array.

6.3 Model Application

The model was used to simulate a non-uniformly spaced array after verification. While the main focus of this thesis was not to determine the ideal array configuration, the model presented in Chapter III provides the ability to evaluate the performance of non-uniformly spaced arrays in airborne radar. Two different circular arrays were simulated using this model, one containing 15 elements and one containing 24 elements. The performance of each circular array was compared to a uniformly spaced 6×6 array. All three arrays had the same width and height. It was found that the circular arrays introduced more interference from the environment than the uniform planar array due to larger sidelobes, fewer nulls, and non-uniform element spacing. However, the three arrays had very similar SINR losses when using the matched filter and JDL algorithms. The circular arrays actually had less SINR loss than the uniform planar array when using the JDL STAP algorithm. The circular arrays had greater SINR loss than the 6×6 array when using the FTS algorithm. Detection probability is difficult to compare between the arrays since they contain different numbers of elements. The 6×6 array has more elements, so it has a higher integration gain than the circular arrays. However, detection probability results indicate JDL performs well with the circular arrays. The FTS method did not perform as well as the JDL method for all three arrays. The circular arrays degraded in output SINR at about the same rate as

81

the uniform planar array for the 10% and 20% element failure rates. All simulation results demonstrate there are potential array configurations which are more efficient than the uniform planar or linear arrays typically used in airborne radar platforms. These potential array configurations could lead to reduced array costs due to fewer elements without sacrificing detection capabilities.

6.4 Future Research

As it stands, the model in Chapter III is valid for linear and planar arrays with arbitrary element spacing. The non-uniformly spaced array model could be modified to include shadowing effects in the 3D conformal array case. Incoming radar waves might not strike every element in the array if it is conformal, so this must be taken into consideration.

The simulations performed in Chapter V primarily demonstrated the model for non-uniformly spaced arrays is valid. There are infinitely many arrays that can be explored, so research should be done to investigate different array configurations. More work is necessary to evaluate performance of each non-uniform array. Detection probability and SINR loss should be evaluated for a variety of scenarios to better characterize overall array performance. Many different target azimuth and elevation angles, Doppler frequencies, and ranges could be considered. The degrees of freedom could also be varied when using each STAP technique.

The non-uniformly spaced array model can be extended to different applications, including space-based radar as one possible extension. Multiple spacecraft form an array in space, where each spacecraft is an element. The space-based radar model will have a few changes that must be made. The clutter model will change since the radar platform is at a much higher altitude. Atmospheric attenuation must also be included for the space-based radar model. The earth's rotation will also be another factor to be considered. There are many different constellations presented in the literature that can be studied.

Appendix A. Kronecker Product

The Kronecker Product is defined in [4] as

$$\mathbf{A} \otimes \mathbf{B} \equiv \begin{bmatrix} A_{11}\mathbf{B} & A_{12}\mathbf{B} & A_{13}\mathbf{B} & \cdots & A_{1M}\mathbf{B} \\ A_{21}\mathbf{B} & A_{22}\mathbf{B} & A_{23}\mathbf{B} & \cdots & A_{2M}\mathbf{B} \\ \vdots & \vdots & \vdots & \vdots & \vdots \\ A_{N1}\mathbf{B} & A_{N2}\mathbf{B} & A_{N3}\mathbf{B} & \cdots & A_{NM}\mathbf{B} \end{bmatrix}.$$

Every element in $\mathbf{A}$ is multiplied by the matrix $\mathbf{B}$. If $\mathbf{A}$ is $N \times M$ and $\mathbf{B}$ is $P \times Q$, then the resulting matrix is $NP \times MQ$.

Bibliography

1. Balanis C. *Antenna Theory* (Second Edition). New York, NY: John Wiley & Sons, Inc., 1997.

2. Brooks L. S. and Reed I. S. "Equivalence of the Likelihood Ratio Processor, the Maximum Signal-to-Noise Ratio Filter, and the Wiener Filter," *IEEE Transactions on Aerospace and Electronic Systems*, 690–692 (September 1972). Correspondence.

3. Corbell P. M. and Hale T. B. "3-Dimensional STAP Performance Analysis Using the Cross-Spectral Metric." *Proceedings of the 2004 IEEE Radar Conference*. 610–615. Philadelphia, PA: IEEE Aerospace and Electronic Systems Society, April 2004.

4. Graham A. *Kronecker Products and Matrix Calculus with Applications*. Ellis Horwood: Mathematics and its Applications, Market Cross House, Cooper Street, Chichester, West Sussex, PO19 1EB, England: Ellis Horwood Limited, 1981.

5. Hale T. B. *Airborne Radar Interference Suppression Using Adaptive Three-Dimensional Techniques*. Ph.D. dissertation, School of Engineering and Management, Air Force Institute of Technology (AETC), 2950 P Street, Bldg 640, Wright-Patterson AFB, OH 45433-7765, June 2002. AFIT/DS/ENG/02-02.

6. Jaffer A., Baker M., Ballance W., and Staub J. *Adaptive Space-Time Processing Techniques for Airborne Radars*. Contract F30602-89-D-0028, Fullerton, CA 92634: Hughes Aircraft Company, July 1991.

7. Klemm R. *Principles of Space-Time Adaptive Processing*, *12*. IEE Radar, Sonar, Navigation and Avionics Series. Michael Faraday House, Six Hills Way, Stevenage, Herts. SG1 2AY, United Kingdom: Institution of Electrical Engineers (IEE), 2002. ISBN 0852961723.

8. Nathanson F. E. *Radar Design Principles: Signal Processing and the Environment* (Second Edition). McGraw-Hill, Inc., 1991.

9. Reed I. S., Mallett J., and Brennan L. "Rapid Convergence Rate in Adaptive Arrays," *IEEE Transactions on Aerospace and Electronic Systems*, *AES-10, No. 6*:853–863 (November 1974).

10. Skolnik M. I. *Introduction to Radar Systems* (Third Edition). 1221 Avenue of the Americas, New York, NY 10020: McGraw-Hill, Inc., 2001. ISBN: 0072881380.

11. Stutzman W. L. and Thiele G. A. *Antenna Theory and Design* (Second Edition). New York, NY: John Wiley & Sons, Inc., 1998.

12. Wang H. and Cai L. "On Adaptive Spatial-Temporal Processing for Airborne Surveillance Radar Systems," *IEEE Transactions on Aerospace and Electronic Systems*, *30*(3):660–669 (July 1994).

13. Ward J. *Space-Time Adaptive Processing for Airborne Radar*. Contract F19628-95-C-0002, Lexington, Massachusetts: Lincoln Laboratory, Massachusetts Institute of Technology, December 1994.

14. Zatman M. "Circular Array STAP." *Proceedings of the 1999 IEEE Radar Conference*. 108–112. April 1999.

15. Zatman M. "Circular Array STAP," *IEEE Transactions on Aerospace and Electronic Systems*, *36*(2):510–516 (April 2000).

REPORT DOCUMENTATION PAGE

Form Approved
OMB No. 0704–0188

1. REPORT DATE *(DD–MM–YYYY)*	2. REPORT TYPE	3. DATES COVERED *(From — To)*
23-03-2006	Master's Thesis	Aug 2004 — Mar 2006

4. TITLE AND SUBTITLE

An Airborne Radar Model For
Non-Uniformly Spaced Antenna Arrays

5a. CONTRACT NUMBER

5b. GRANT NUMBER

5c. PROGRAM ELEMENT NUMBER

6. AUTHOR(S)

Matthew V. Young, 2d Lt, USAF

5d. PROJECT NUMBER

5e. TASK NUMBER

5f. WORK UNIT NUMBER

7. PERFORMING ORGANIZATION NAME(S) AND ADDRESS(ES)

Air Force Institute of Technology
Graduate School of Engineering and Management (AFIT/EN)
2950 Hobson Way
WPAFB OH 45433-7765

8. PERFORMING ORGANIZATION REPORT NUMBER

AFIT-GE-ENG-06-58

9. SPONSORING / MONITORING AGENCY NAME(S) AND ADDRESS(ES)

AFRL/SNRT (AFMC)
Attn: Mr. William Baldygo
26 Electronic Parkway
Rome, NY 13440   DSN: 587-3576   William.Baldygo@wpafb.af.mil

10. SPONSOR/MONITOR'S ACRONYM(S)

11. SPONSOR/MONITOR'S REPORT NUMBER(S)

12. DISTRIBUTION / AVAILABILITY STATEMENT

Approval for public release; distribution is unlimited.

13. SUPPLEMENTARY NOTES

14. ABSTRACT

This thesis presents an airborne radar model for non-uniformly spaced antenna arrays. Non-uniform arrays potentially possess advantages unobtainable by uniformly spaced arrays. An element position matrix is defined to accommodate arbitrary element locations. The new element position matrix affects the time/phase delay to each element, spatial frequencies, steering vectors, space-time snapshots, and covariance matrices. The joint domain localized and factored time-space space-time adaptive processing algorithms are also updated so they are compatible with the new model. The non-uniformly spaced array radar model is verified with previous models presented by Jaffer, Ward, and Hale. The model for non-uniform arrays is used to compare performance of 24 element and 15 element circular arrays to a 6×6 uniformly spaced planar array having the same physical dimensions. Simulation results indicate that non-uniformly spaced arrays such as the circular array can potentially be used in airborne radar systems in place of uniformly spaced arrays. As a result, array costs may be reduced by using fewer elements without sacrificing detection capabilities.

15. SUBJECT TERMS

airborne radar, radar antennas, nonuniform, arrays, circular antennas

16. SECURITY CLASSIFICATION OF:			17. LIMITATION OF ABSTRACT	18. NUMBER OF PAGES	19a. NAME OF RESPONSIBLE PERSON
a. REPORT	b. ABSTRACT	c. THIS PAGE			Maj. Todd B. Hale (ENG)
U	U	U	UU	101	19b. TELEPHONE NUMBER *(include area code)* (937) 255–3636, ext 4639; e-mail: Todd.Hale@afit.edu

Standard Form 298 (Rev. 8–98)
Prescribed by ANSI Std. Z39.18